Journal of Structural Geology 191 (2025) 105314

Contents lists available at ScienceDirect

Journal of Structural Geology

journal homepage: www.elsevier.com/locate/jsg

Thrust vs. fold nappes: Mechanical and geometrical controls from 2D numerical simulations and applications to a recumbent fold of the Pyrenees

Marc Guardia [a,*], Albert Griera [a], Boris J.P. Kaus [b], Andrea Piccolo [c], Norbert Caldera [a,d], Antonio Teixell [a]

[a] Departament de Geologia, Universitat Autònoma de Barcelona, 08193, Bellaterra, Barcelona, Spain
[b] Institute for Geosciences, Johannes-Gutenberg University of Mainz, 55128, Mainz, Germany
[c] Bayerisches Geoinstitut, Universität Bayreuth, 95440, Bayreuth, Germany
[d] Institut Geològic i Cartogràfic de Catalunya, 08038, Barcelona, Spain

ARTICLE INFO

Keywords:
Thrust nappe
Fold nappe
Mechanical stratigraphy
Numerical modelling
Pyrenees

ABSTRACT

Thrust and fold nappes are found in the internal and external portion of orogenetic belts, and have been the subject of geometric and kinematic characterization during the last century. In spite the extensive studies, there is still not a full understanding of the processes and properties that favour thrusting over folding and vice versa. We address this issue by numerical modelling with application to a natural case of the Pyrenees, the Eaux-Chaudes massif, an Alpine fold-and-thrust structure in the western Axial Zone. The Eaux-Chaudes structure consists of a basement-cored recumbent fold nappe with a large reverse limb in ductilely-deformed Upper Cretaceous carbonates, transitioning laterally to the east to an imbricate thrust fan that also exhibits ductile deformation to the east. The spatio-temporal association of these structural styles at Eaux-Chaudes can be a consequence of the pre-orogenic configuration and highlights the need to investigate under which conditions and precursor geometries one or the other nappe style are favoured. Here, we present a systematic numerical modelling study of the variability in the initial mechanical and geometrical conditions, using the thermo-mechanical staggered finite-difference code LaMEM. We also investigate the mechanism that favour the potential migration of fold hinges and lead to the preservation of layer thickness in the reverse fold limbs, and quantify it with a new nondimensional parameter, the localisation index (I_{loc}).

Our results demonstrate the need of a stiff forestop for nappe development. The absence of a forestop causes detachment buckle folds in the strong layers. Deep burial and the combination of a thick upper decoupling unit and a lower detachment level are essential features favouring viscous behaviour and spatially distributed deformation, enabling recumbent folding by progressive hinge migration, and characterized by low and stable values of I_{loc}. On the other hand, shallower conditions, short lengths of the stiff layer and lower friction angles inhibit hinge migration. Instead, they enhance instead reverse limb stretching and shearing, which eventually results in strain localisation and thrusting. These are characterized by a moderate-to-quick rises of I_{loc}. Our results may be applicable to other orogenic belts and to other parts of the Axial Pyrenean hinterland where the Mesozoic cover has been eroded and the Alpine deformation is obscure.

1. Introduction

The pre-orogenic mechanical and geometrical architecture of the collided margins controls the evolution of fold and thrust systems resulting from inversion tectonics in orogenic belts. This architecture depends on the previous geodynamic evolution within the Wilson cycle (e.g., Manatschal et al., 2021), including ancient collisions, rifting, thermal subsidence, basin infill, etc. Mechanical heterogeneities, due to the diverse rheology of the involved rocks or to inherited faults and drive the mechanical behaviour during subsequent orogenic deformation (e.g., Welbon, 1988; Butler et al., 2006, 2018; Bellahsen et al., 2012; Zerlauth et al., 2014). For example, the presence of stiff plutonic bodies or faults that act as buttresses can exercise a control on the structural style by focusing the deformation (e.g., Bucher, 1956; Wissing and Pfiffner, 2003; Bauville and Schmalholz, 2017; Kiss et al., 2020; Spitz et al., 2020). On the other hand, weak layers such as shales or evaporites

* Corresponding author.
E-mail address: marc.guardia@uab.cat (M. Guardia).

https://doi.org/10.1016/j.jsg.2024.105314
Received 30 July 2024; Received in revised form 28 November 2024; Accepted 28 November 2024
Available online 6 December 2024

act as detachment horizons for contractional structures, facilitating the strong layers (e.g., limestones, sandstones) to travel long distances over autochthonous terrains (e.g., Pfiffner, 1993) in thrust- or fold-nappes (e.g., Pfiffner, 1993; Epard and Escher, 1996; Erickson, 1996; Costa and Vendeville, 2002).

Previous field observation-based studies highlight that geometrical factors, such as the alternation of weak and strong sedimentary layers and their relative thickness, are key mechanical players in the development of thrust- and fold-nappes. Thus, when weak layers are relatively thick compared to strong ones, they promote the overall folding of strong layers over thrusting (e.g., Pfiffner, 1993; Epard and Escher, 1996; Erickson, 1996; Costa and Vendeville, 2002).

Thrust nappes (or thrust sheets) and fold nappes could be considered as the two end-member forms of tectonic superposition driven by compression. Dennis et al. (1981) described thrust nappes as allochthonous sheets over a localized, thin basal thrust surface. These sheets display a short or non-existent reverse limb (Fig. 1A) and are commonly associated with upper crustal conditions. Conversely, fold nappes qualify as allochthonous units showing large-scale overturned or recumbent limbs (km-scale), often developed deeper in the crust (e.g., Ramsay, 1980; Epard and Escher, 1996; Bastida et al., 2014; Fig. 1B). Fold nappes are associated with more distributed deformation, dominated by ductile-viscous behaviour, and exhibit sub-horizontal axial planes and often long and stretched recumbent limbs that may be sheared out into basal thrusts or shear zones.

Although the geometry and kinematics of fold nappe structures are well documented after more than a century of studies (e.g., Lugeon, 1902; Heim, 1906, 1919–1922, Termier, 1906; Argand, 1916; Ramsay, 1980; Escher et al., 1993; Epard and Escher, 1996; Fernández et al., 2007; Bastida et al., 2014; Pfiffner, 2014), their mechanical controls are still under discussion (e.g., Bauville and Schmalholz, 2017; Spitz et al., 2020; Kiss et al., 2020), with remaining issues such as the folding mechanisms that facilitate the development of km-scale overturned limbs (Fig. 1C).

The goal of this work is to study the influence of the tectonic inheritance (i.e. initial configuration), the mechanical stratigraphy (i.e., material properties and their contrasts) and the rheology (e.g., brittle/frictional vs. viscous) on thrust/fold nappe development (Fig. 1C), based on numerical modelling and applying the results to the Eaux-Chaudes fold-thrust structure in the Pyrenees (Caldera et al., 2023). We also address and quantify the mechanisms under which a km-scale overturned limb can be developed, contrasting the two potential viable mechanisms: fixed hinge and stretching vs. hinge migration and rigid limb rotation (e.g. Perrin et al., 2013).

2. Fold nappes vs. thrust nappes

Recumbent folds or fold nappes are usually interpreted as formed in wide zones of simple shear deformation in compressional settings (Bastida et al., 2014). A determinant parameter in their development is the original orientation of strong rock layers with respect to the shear zone margins (e.g., Ramsay et al., 1983; Dietrich and Casey, 1989; Carreras et al., 2005; Llorens et al., 2013). If the layer orientation is parallel to the shear zone boundaries (that is, an orientation without shortening parallel to the layer in simple shear) and if they are surrounded by weaker rocks (i.e. such as a stiff single-layer immersed in a weak matrix), an initial buckling instability or an inherited perturbation is required to produce folding (e.g. Bucher, 1956; Ramsay et al., 1983; Dietrich and Casey, 1989; Carreras et al., 2005). Once nucleated, folds start with axial planes at high angle to the layering and the shear direction and can evolve into recumbent folds as the shearing progresses with time (e.g., Ez, 2000). This case requires a significant amount of strain before attaining a large fold amplification. For cases in which the initial angle between the strong layer and the shear zone is oblique, the required strain is reduced (Bastida et al., 2014). Subsequent kinematic evolution within the simple shear zone can produce the stretching of the

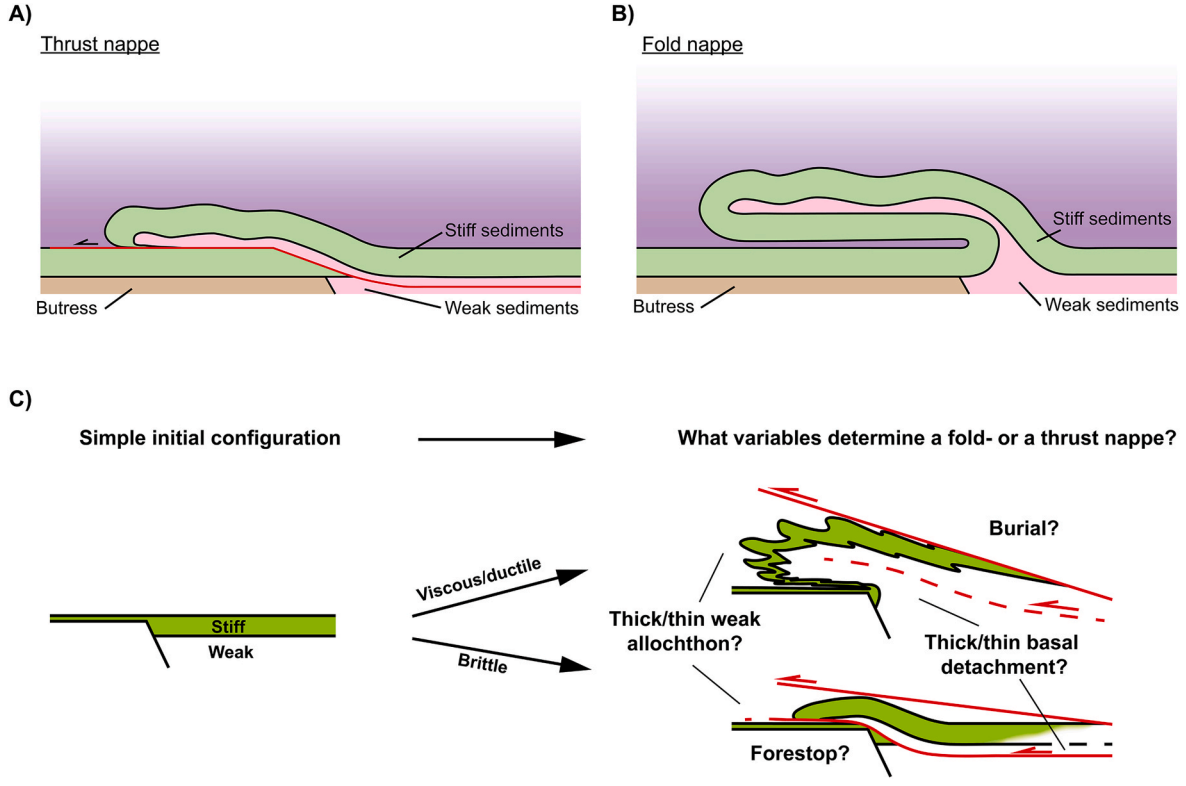

Fig. 1. Simplified sketch of the geometrical features of an idealized thrust nappe **(A)** and a recumbent fold nappe **(B),** end-members resulting from tectonic shortening. **(C)** Sketch of an alternance of stiff and weak layers within a thick shear zone indicating the variables that could determine the dominant frictional-plastic/brittle or viscous/ductile behaviour and therefore, the resulting structural style.

reverse fold limb (Bastida et al., 2014). However, in this situation, the fold hinges are fixed in the material (i.e., non-mobile hinges) after the initial buckling, and stretching is the only method to increase the limb length (e.g., Mancktelow, 1999; Frehner, 2011), which may result in the shearing out of the recumbent limb during late phases of evolution.

Alternatively, Perrin et al. (2013) on the basis of analogue modelling proposed that large, overturned limbs of fold nappes could form by progressive fold hinge migration. This implies that material particles are travelling with time between structural positions within the fold. In their models, progressive shift, rotation, and unfolding of the syncline formed during the early stages of a paired fold system (i.e., an anticline-syncline pair with a reverse limb in between), controlled the growth of an overturned fold limb. This situation leads to rigid rotation of the strong layers and tends to preserve the original layer thickness. Perrin et al. (2013) aimed to model the thrust and fold propagation in their setup, focusing on foreland basins with moderate burial conditions and effective detachment levels. If a forestop condition is added, it tends to favour the migration of anticline hinges, because the syncline is fixed by the strain shadow created by the stiff forestop; otherwise, the progressive migration of the syncline hinge will produce buckle folds (e.g., Epard and Groshong, 1995; Homza and Wallace, 1995, 1997; Poblet and McClay, 1996; Perrin et al., 2013; Poblet, 2020).

Recently, Caldera et al. (2021) described a basement-involved fold nappe structure affecting the tabular Mesozoic sedimentary lid in the Eaux-Chaudes Area (western Axial Zone of the Pyrenees, France; Fig. 2A and B). For this case, it is not appropriate to invoking the ductile closure and extrusion of previous extensional basins, as proposed for the Helvetic nappes of the Alps along thick basement shear zones (e.g. Belhassen et al., 2012; Spitz et al., 2020).

Furthermore, the Eaux-Chaudes nappe constitutes a unique natural laboratory to investigate the variables favouring the occurrence of thrust nappes or fold nappes, and to gain insight into the meaning of the structural variations observed by Caldera et al. (2021) in terms of rheology and mechanical stratigraphy (Fig. 1C).

3. Geological setting of the Eaux-Chaudes natural case

The Pyrenees are an asymmetric doubly-verging orogenic wedge (e.g. Choukroune and ECORS Team, 1989; Muñoz, 1992; Teixell, 1998) developed during the Late Cretaceous-Early Miocene Alpine orogeny from the inversion of a hyperextended rift system. After the late Paleozoic Variscan orogeny, rifting occurred in the Pyrenean domain in two main episodes during the Permian-Triassic and the early Cretaceous, culminating in mantle exhumation during the Albian-Cenomanian (Jammes et al., 2009; Lagabrielle et al., 2010). The late Cretaceous encompassed a short post-rift stage which often produced expansive, tabular deposits, followed by the initial orogenic inversion starting in mid Santonian times (ca. 84 Ma).

During the first stages of the Pyrenean orogeny, the deformation in the west-central Pyrenees was largely accommodated by thin-skinned thrusting while the exhumed mantle tract subducted, favoured by weak layers (mainly Triassic evaporites and shales) acting as a detachment levels (e.g., Lakora thrust and Chaînons Béarnais Belt; Labaume and Teixell, 2020). Later convergent deformation progressively involved collision of the rifted margins, stacking and uplifting the Iberian basement in the Pyrenean Axial Zone.

The Eaux-Chaudes massif is an Upper Cretaceous inlier surrounded by Paleozoic basement rocks in the northwestern Axial Zone (Ternet, 1965). In its western part, in the Ossau valley, the Eaux-Chaudes structure consists of a km-scale south-verging, basement-cored recumbent fold outlined by Upper Cretaceous carbonates (Caldera et al., 2021, 2023; Fig. 2A and B). Folding is inferred to happen during the early and mid-Eocene before the emplacement of the underlying Gavarnie thrust that uplifts the whole Axial Zone in the west-central Pyrenees (Labaume et al., 2016). The stratigraphic succession (Fig. 3) consists of Upper Cretaceous platform carbonates resting directly on top of Paleozoic low-grade metasedimentary rocks and granodiorites. Along the unconformity between the Paleozoic basement and the Upper Cretaceous, occasionally Lower Triassic Buntsandstein conglomerate pods are preserved (Ternet, 1965), allowing to constraint the polarity of the Mesozoic sequence wherever deformed. The Upper Cretaceous carbonates, of Cenomanian to Santonian age, represent a shelf in the proximal margin of the Iberian plate during the Pyrenean post-rift stage. They are followed by sandstone-shale flysch deposits of Campanian-Maastrichtian age (Ternet, 1965), recording flexural subsidence in the first stages of the Pyrenean orogeny (Teixell, 1993).

The Paleozoic metasedimentary sequence consists of Silurian weak unit mainly composed of black slates, and a thick succession of Devonian to Upper Carboniferous stiff limestones and sandstones. A late Carboniferous granodiorite, the Eaux-Chaudes pluton (ECP), intruded these rocks. Together with the Upper Cretaceous autochthonous succession immediately above, it exhibits low deformation during the Alpine orogeny (Fig. 2B).

The Eaux-Chaudes fold nappe in the Ossau valley is ~9 km long recumbent and detached on the Silurian slates, with a flat-lying overturned limb (apparently preserving its thickness) showing ductile deformation in the Upper Cretaceous carbonates (Caldera et al., 2021, 2023). RSCM paleothermometry indicates maximum paleotemperatures of ~350 °C for the recumbent limb of the Eaux-Chaudes structure (greenschist facies), consistent with mylonitic foliation and lineation observed. On the other hand, the normal limb (which displays second order open folds) reached temperatures of 310 °C. Caldera et al. (2021) estimated the burial at 8–10 km, but this comes with large uncertainty because of the challenge of evaluating past geothermal gradients. The Upper Cretaceous overturned limb is in mechanical contact over an autochthonous Cretaceous cover with similar stratigraphy, attached to the ECP underneath. Small Upper Triassic remnants are pinched in the mechanical contact between the recumbent limb and the autochthonous succession, drawing a tight syncline between the overturned limb and the latter (Caldera et al., 2021, 2023). The fold structure shows a marked strain increase towards the overturned limb, and from south to north. In the eastern part of the massif, the Eaux-Chaudes fold nappe passes laterally via a transfer zone to a ductile fold-thrust fan, and the recumbent fold is no longer recognized (Caldera et al., 2023). The Eaux-Chaudes massif is in turn overlain by the Lakora thrust units, a series of allochthonous sheets that carry Palaeozoic metasediments and remnants of its Triassic cover (Buntsandstein and Keuper facies), as well as Albian conglomerates (subsequently called North Pyrenean units) (Fig. 2B). To the north, these units are thrust by the Chaînons Bearnais belt (CBB), a fold-thrust system involving Jurassic to Aptian carbonates and Albian-Upper Cretaceous flysch deposits detached on the Upper Triassic evaporites, affected by diapirism (Teixell et al., 2016; Labaume and Teixell, 2020).

4. Methods

4.1. Numerical method

We use the 3-D thermomechanical staggered finite differences code LaMEM (Kaus et al., 2016) to perform 2D parametric numerical simulations to investigate the controlling factors and changes in the deformation style between thrust nappes (plastic/brittle-localisation) and recumbent fold nappes (viscous/ductile-distributed). Drawing on the concept of continuum mechanics (e.g., Mase and Mase, 1970; Turcotte and Schubert, 2014) the LaMEM code solves partial differential equations that describe rock deformation.

The mechanical problem is defined by the conservation of mass and linear momentum equations:

$$\frac{\partial v_i}{\partial x_i} = 0, \tag{1}$$

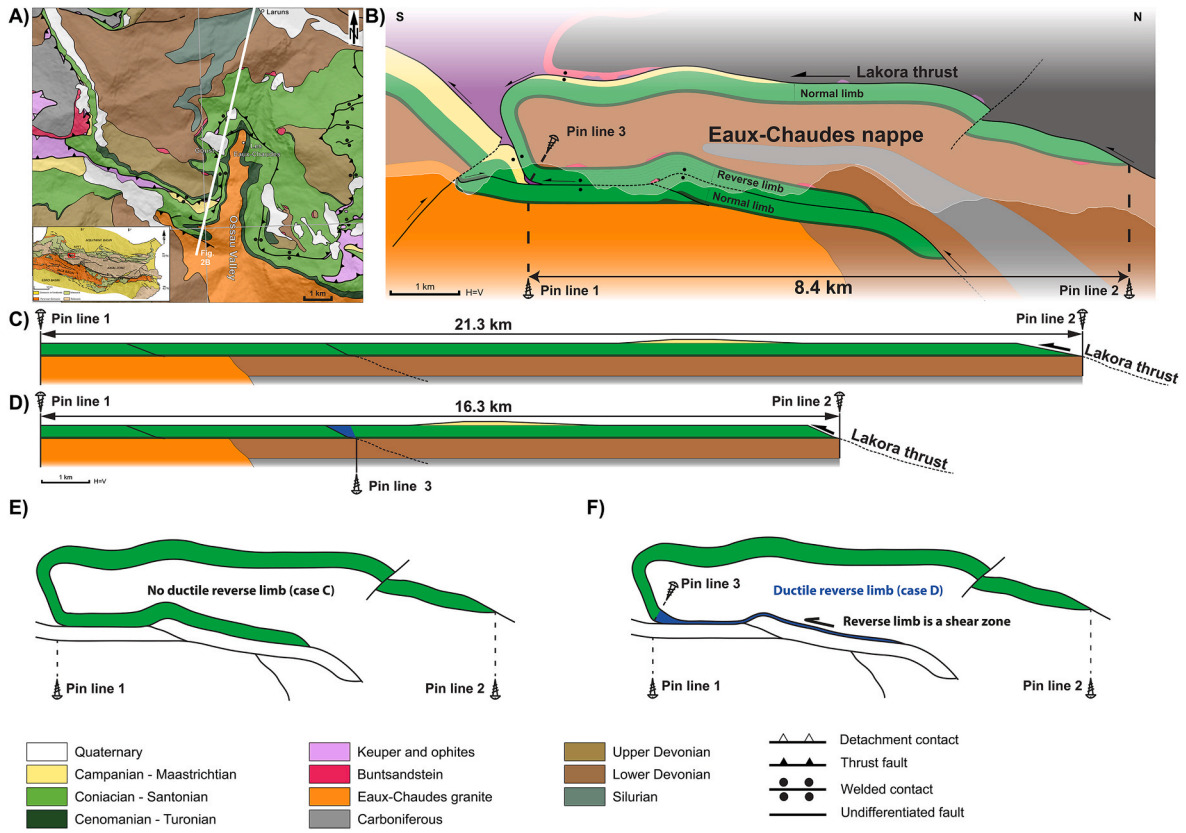

Fig. 2. **A)** Geological map of the western Eaux-Chaudes massif in the Ossau valley of the French Pyrenees (Caldera et al., 2021). **B)** Cross section of the Eaux-Chaudes recumbent fold nappe in the western side of the Ossau valley (see Fig. 2A for location) (Caldera et al., 2021). **C)** Restored section of the Eaux-Chaudes fold nappe assuming no ductile stretching of the overturned limb (i.e., formed by a migrating fold hinge). **D)** Alternative restored version considering the entire overturned limb as a product of ductile stretching (i.e., blocked or reduced-mobility hinge). **E) and F)** End-member options to constrain minimum/maximum length of the Upper Cretaceous cover due to the uncertainty of ductile deformation. Sketch of the non-ductile overturned limb end-member case shown in C, assuming that there is no ductile stretching in the overturned limb (**E**). Sketch of the entirely-ductile overturned limb end-member case shown in D, assuming that the whole overturned limb (blue path) is product of the ductile stretching (**F**). (For interpretation of the references to colour in this figure legend, the reader is referred to the Web version of this article.)

$$-\frac{\partial P}{\partial x_i}+\frac{\partial \tau_{ij}}{\partial x_j}=\rho g_i, \tag{2}$$

where x_i is the Cartesian coordinate system (x,y,z), v_i is the component of the velocity vector, P is pressure, $\tau_{ij}=\sigma_{ij}+P\delta_{ij}$ represents the components of the deviatoric Cauchy stress tensor (δ_{ij} is the Kronecker delta), ρ is density and g_i is the gravity vector with a value of [0, 0, 9.8] m/s^2 (z is the vertical orientation in the models).

The simulations were performed using linear and non-dependent on temperature visco-elasto-plastic rheology, where the resultant deviatoric strain rate tensor $\dot{\varepsilon}_{ij}$ is obtained from the sum of the elastic $\left(\dot{\varepsilon}_{ij}^{el}\right)$, viscous $\left(\dot{\varepsilon}_{ij}^{vs}\right)$, and plastic $\left(\dot{\varepsilon}_{ij}^{pl}\right)$, components of the deviatoric strain rate tensor,

$$\dot{\varepsilon}_{ij}=\dot{\varepsilon}_{ij}^{el}+\dot{\varepsilon}_{ij}^{vs}+\dot{\varepsilon}_{ij}^{pl}=\frac{\tau'_{ij}}{2G}+\frac{\tau_{ij}}{2\eta_{eff}}+\dot{\varepsilon}_{II}^{pl}\frac{\tau_{ij}}{\tau_{II}}, \tag{3}$$

where $\tau'_{ij}=\frac{\partial \tau_{ij}}{\partial t}+\tau_{ik}\omega_{kj}-\omega_{ik}\tau_{kj}$ is the Jaumann objective stress rate and $\omega_{ij}=\frac{1}{2}\left(\frac{\partial v_i}{\partial x_j}-\frac{\partial v_j}{\partial x_i}\right)$ is the spin tensor; G is the elastic shear modulus; η_{eff} is the effective viscosity; and τ_{II} is the second invariant of the stress tensor; $\tau_{II}=\left(\frac{1}{2}\tau_{ij}\,\tau_{ij}\right)^{1/2}$.

The magnitude of the plastic strain rate $\left(\dot{\varepsilon}_{II}^{pl}\right)$ is determined by applying the Drucker-Prager criterion for plasticity:

$$\tau_{II}\le\tau_Y=\sin(\phi)P+\cos(\phi)c, \tag{4}$$

where τ_Y is the yield stress, ϕ is the friction angle, P is the pressure and c the cohesion.

The open-source code LaMEM[1] solves the system of equations using a staggered-grid finite-difference discretization. A marker-in-cell method advects the material properties, and the sticky air approach implements a free surface.

4.2. Model setup

The structure of the Eaux-Chaudes fold nappe originally proposed by Caldera et al. (2021) is shown in Fig. 2B. Assuming plane strain, transport parallel to the cross-section, and line-length balancing, we performed a first-order restoration of the fold structure. In light of the uncertainties of these assumptions and of the amount of ductile deformation experienced by the overturned limb (e.g., Caldera et al., 2023), we considered two end-member options for the restoration to constrain the minimum/maximum length of the Upper Cretaceous cover. One option assumed no stretching of the recumbent limb (Fig. 2C and E), which gave a restored Upper Cretaceous panel 21.3 km long and 12.8 km of shortening (60%). The second option assumed the formation of the entire recumbent limb by ductile/brittle simple shear (Fig. 2D and

[1] https://github.com/UniMainzGeo/LaMEM.

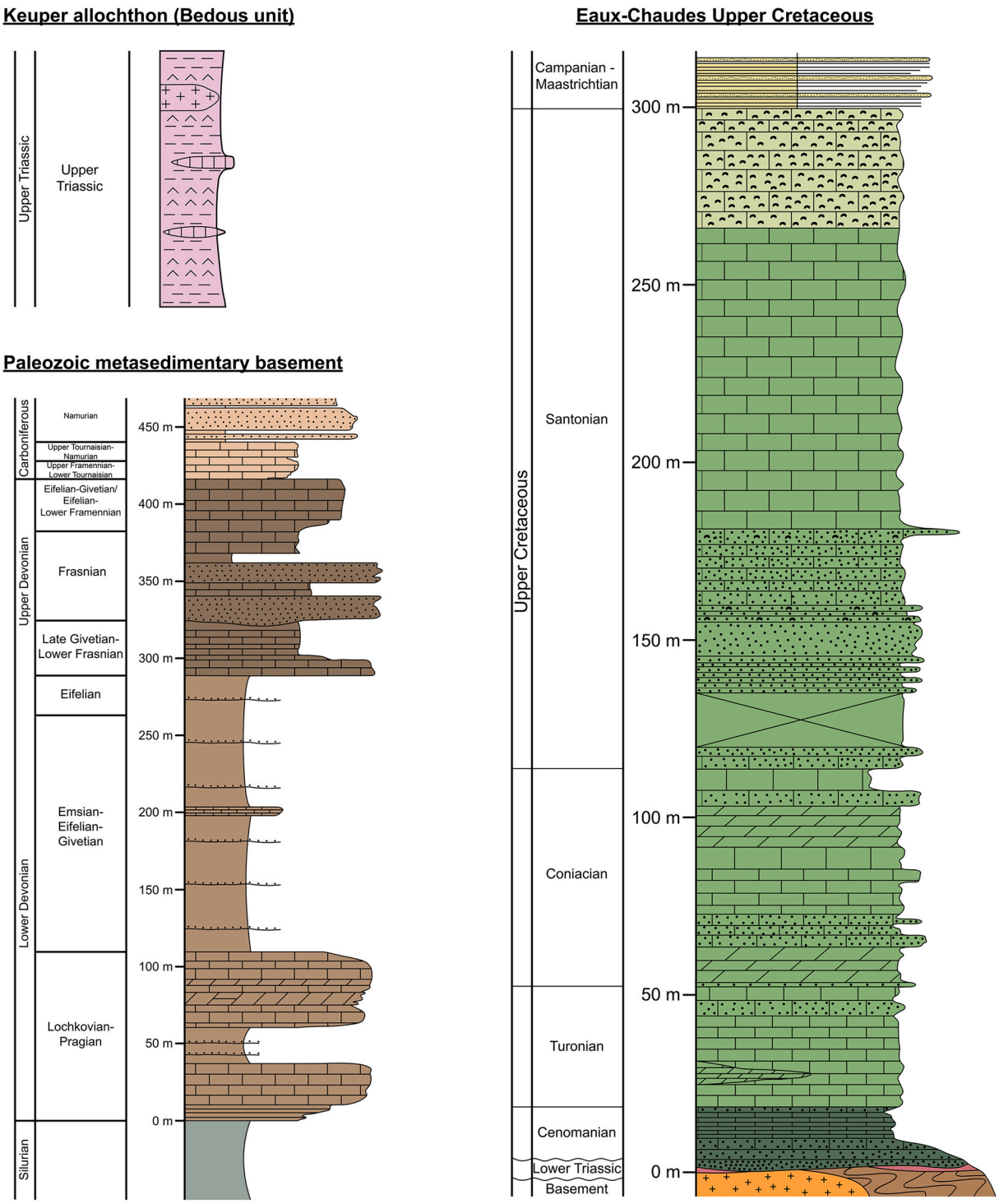

Fig. 3. Synthetic stratigraphic logs of the Eaux-Chaudes massif and surrounding units (modified from Caldera, 2022).

F). For the more extreme scenario, it implies a discrete shear zone and offset between layer cut-offs, resulting in a restored Upper Cretaceous length of 16.3 km and a shortening of 7.8 km (48%).

Fig. 4 displays the initial setup of the reference model. Based on the restored dimensions, the reference model consists of a 85 × 11 km model box with a numerical resolution of 256 × 136 (X and Z directions) elements, and a refinement of the mesh in the Z direction in the bottom part of the model (128 elements between -8 km $< Z < -0.5$ km). The model is divided into two domains separated by the Lakora thrust detachment level of the allochthonous nappes (Fig. 4). The hanging wall represents the allochthonous nappes of the Lakora and the North Pyrenean nappes, soled by Keuper rocks (i.e., allochthonous Paleozoic-bearing upper thrust sheets and Mesozoic rocks of the CBB), while the footwall includes two subdomains representing the future Eaux-Chaudes fold nappe and its autochthonous footwall (Fig. 4B). We prescribed the Lakora detachment as a weak mechanical layer with a flat-ramp-flat geometry (Figs. 2 and 4). In the reference model, the angle of this ramp is $\beta = 10°$. The upper and lower allochthonous nappes (AN) are defined as moderate strong units between 8 and 6.6 km of maximum and minimum thicknesses (Fig. 4) to simulate the North Pyrenean nappes. Both are

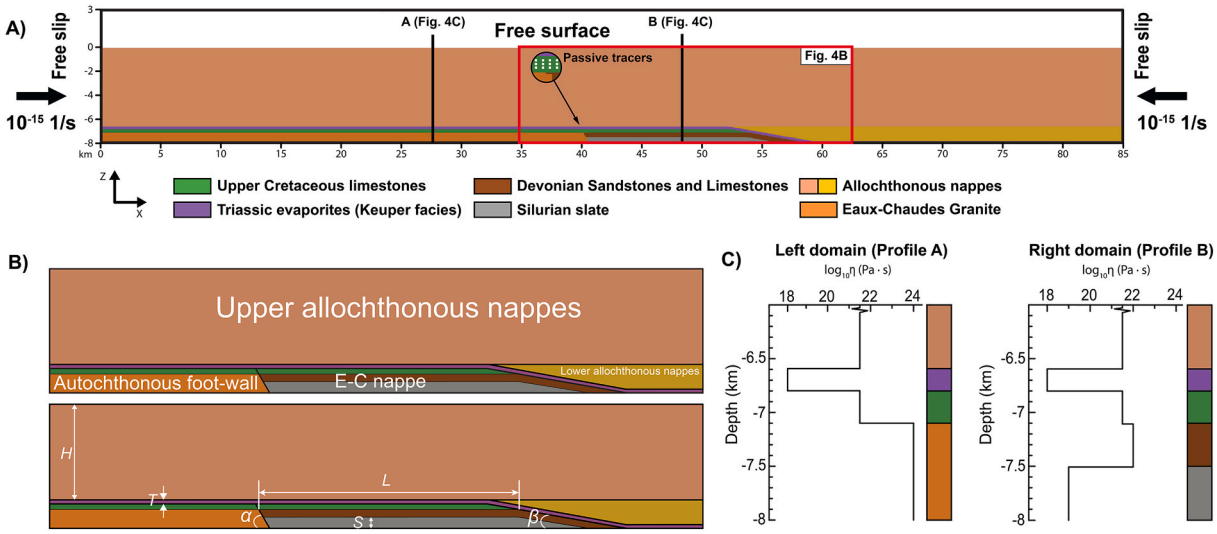

Fig. 4. **A)** Initial setup of the reference simulation. Numerical resolution is 256 × 136 (X x Z) grid points. We applied a mesh refinement of 128 grid points between Z = −0.5 km and Z = −8km, and 8 grid points for Z > −0.5 km. A free-slip boundary condition has been applied in the left and the right sides and a free surface at the top of the initial setup. **B)** Structural units of the Eaux-Chaudes massif represented in the reference model. **C)** Vertical profiles of viscosity showing the vertical and horizontal mechanical contrasts for the domains on the left and the right sides in the simulations.

mechanically equivalent (Table 1), and they are distinguished by having a reference point to track the advancing upper allochthonous. The Paleozoic rocks of the Eaux-Chaudes nappe form a pile of layers with inherited gentle arching, simplified to a north-dipping kink (Fig. 4A and B; Caldera et al., 2023). The pile is composed of a basal weak material of 0.5 km thick to represent the Silurian black slates (grey colour Fig. 4B), and a layer of 0.4 km thickness to represent the Devonian-Carboniferous metasedimentary rocks (dark brown). The autochthonous footwall was defined as a stiff unit of 0.9 km thickness mimicking the Eaux-Chaudes granodioritic pluton. The boundary between both Paleozoic subdomains was assumed to be steeply dipping ($\alpha = 60°$). Finally, on top of both subdomains a layer of 0.3 km thickness was defined to represent the unconformable Upper Cretaceous limestone (green). On top of this initial setup, there is a 3 km thick low viscosity air layer with a free surface condition. A total of seven distinct units (mechanically and internally homogeneous) were thus used, eight considering the low viscosity air unit (Table 1).

From the reference model, named "*Rs*" (Fig. 4B), we tested several mechanical and geometrical variables. The mechanical variables include the viscosity (η_{UC}), cohesion (c_{UC}), and friction angle (ϕ_{UC}) of the Upper Cretaceous unit, along with the viscosity (η_{AN}) of the upper allochthonous thrust sheets. The geometrical variables encompass the thickness (T) of the Lakora weak detachment layer (Keuper), the stiffness of the autochthonous basement unit (i.e., the Eaux-Chaudes granite), the thickness of the overburden (H) by allocthonous nappes, the thickness of the Silurian weak layer (S), the angle of the Lakora footwall ramp (β), the angle of the contact between Paleozoic subdomains (α), and the length (L) of the Upper Cretaceous. Tables 1 and 2 list the values for the geometrical and mechanical parameters of each simulation, in which subscripts indicate the values of the modified properties. The range of studied values for the different parameters appears between parentheses. For the case of Silurian rocks, characterized by a small grain size and a high content of phyllosilicates, we followed the results from Niemeijer and Spiers (2005) and Wallis et al. (2015) where very low friction angles are observed in the experiments.

In the initial setup, a free-slip boundary condition was applied to the left and right sides of the models to allow free vertical displacements and a constant strain rate of 10^{-15} s^{-1} from both sides of the model (Fig. 4A).

Table 1
List of the mechanical properties used for each unit in the simulations, based on the geology of the Eaux-Chaudes massif. ρ: density; G: shear modulus; η: viscosity; c: cohesion; ϕ: friction angle.

Unit	ρ (kg/m^3)	G (GPa)	η (Pa·s)	c (MPa)	ϕ (°)
Granite	2800	10	10^{24}	50	30
Silurian slate	2500	10	10^{19}	1	5
Devonian sandstone and limestone	2700	10	10^{22}	1	30
Keuper	2500	10	10^{18}	1	5
Upper Cretaceous	2700	10	5×10^{21}	10	30
Upper North Pyrenean nappe	2700	10	5×10^{21}	1	30
Lower North Pyrenean nappe	2700	10	5×10^{21}	1	30

Table 2
List of geometrical and mechanical variables and values used in each simulation. A sketch of the geometrical variables listed can be found in Fig. 4B. Geometrical variables: H: thickness of the overburden; T: thickness of the upper weak layer; L: length of the Upper Cretaceous panel; β: angle of the Lakora footwall ramp; α: angle of the autochthonous E-C granite; S: thickness of the lower Silurian weak layer. Mechanical variables: η_{UC}: viscosity of the Upper Cretaceous panel; ϕ_{UC}: friction angle of the Upper Cretaceous panel; c_{UC}: cohesion of the Upper Cretaceous panel; η_{AN}: viscosity of the allochthonous nappes.

Variable	Reference
η_{UC} (Pa·s)	5×10^{21} ($1{\cdot}10^{22}$)
c_{UC} (MPa)	10 (1–100)
ϕ_{UC} (°)	30 (5–30)
η_{AN} (Pa·s)	$5{\cdot}10^{21}$ ($1{\cdot}10^{22}$)
T (m)	200 (0–400)
H (km)	6.6 (3–10)
S (m)	500 (300–700)
β (°)	10 (20–90)
α (°)	60 (10–90)
L (km)	14 (10–22)

4.3. Evaluation of the grade of localisation and hinge migration

We assessed the deformation of the Upper Cretaceous layer to constrain the geometrical differences between thrust and fold nappes. This assessment involved tracking the position of a passive tracer grid, defined by 400 × 3 markers in the X and Z directions (Figs. 4A and 5). For all simulations, we keep constant the initial distance between consecutive tracers ($l_0 = 0.13$ km).

Determining the degree of strain localisation in the Upper Cretaceous layer involves using a localisation index (I_{Loc}), defined following the localisation factor proposed by Sornette et al. (1993) as:

$$s = \frac{l}{l_0}, \tag{5}$$

$$I_{Loc} = 1 - \left[\left(\frac{\sum s \cdot \sum s}{\sum s^2}\right)\frac{1}{N}\right], \tag{6}$$

where l is the current length between two consecutive passive tracers, l_0 is the initial length, s is the stretching and N the number of tracers (for a better understanding see section 6.1). I_{Loc} ranges between 0 and 1, ranging from a homogenous distribution of the deformation ($I_{Loc} \sim 0$) to maximum localisation of deformation in a single level ($I_{Loc} = 1$). The analysed area was defined between two reference points defined by 1) the cut-off of the E-C nappe and the autochthonous zone (orange point in Fig. 5A) and 2) the Lakora thrust cut-off (blue dot in Fig. 5A). The systematic evaluation of I_{Loc} occurs every 10 timesteps, within a bulk shortening range from 21.5% (equivalent to 7.6 Ma of simulation time) to 46.2% (equivalent to 19.6 Ma of simulation time).

On the other hand, we also tracked the variation of fold limb length and the position of hinges during simulations and tested the potential migration of fold hinges, as proposed by Perrin et al. (2013). We define the hinge migration as the travelling of material particles between different structural elements in a fold (i.e., fold hinge and limbs). The simplest case is the migration of the hinge through the normal limb, producing an increase of the length of the reverse limb. To quantitatively constrain this process, the method relies on tracking the relative position of the final fold inflexion (IA) observed in the last step of the simulation during all the incremental steps. The IA of the curvilinear recumbent anticline was defined as the point with maximum dip angle (IA; green dot in Fig. 5B), which marks the transition from the normal to the reverse limb. Then, we tracked the material position of the final point IA throughout all the deformation stages (Fig. 5C). For each deformation increment, the current inflexion point was identified (IAc; red dot in Fig. 5C) and three distances were measured: 1) the length of the normal limb, which in the models represents the horizontal distance between the IAc and the Lakora footwall cut-off (NLd; blue dot in Fig. 5B and C), 2) the length of the reverse limb, which represents the horizontal distance from the IAc to the footwall of the fold nappe (ISd; orange dot in Fig. 5B and C), and finally, 3) the horizontal distance between the current IAc and the final IA (IAd; Fig. 5C). The location of the IAc at each time step was defined as the origin of coordinates to graphically represent the evolution of these distances (Fig. 5B and C). Note that during progressive fold growth, the IA represents a material point located in the normal limb that in the last step of the simulations is the inflection point of the anticline fold. Additionally, to quantify the effect of plastic deformation in the reverse limb, we used the I_{Loc} to divide the reverse limb into two segments (labelled by RL and P, and where IS = P + RL; Fig. 5B and C) in function of whether the I_{Loc} of the segments was higher or lower than a threshold value (I_{Loc} >0.15; justified in the discussion section). The distance between the IAc and the first marker, which implies a bulk I_{Loc} higher than 0.15, constitutes the segment RL. On the other hand, the segment P is the complementary length up to the footwall of the fold nappe (i.e. P= IS-RL).

5. Modelling results

We firstly present the results of the reference simulation based on the initial configuration described above (Fig. 6). Then, we describe the results of the systematic variation of our input parameters (Tables 1 and 2; Figs. 7–9).

The results are evaluated to reproduce the first-order features of the recumbent folding of the Eaux-Chaudes nappe, which are: (1) a flat-lying, kilometric scale overturned limb with thickness preserved/constant, (2) a sub-horizontal axial plane, (3) a normal limb with second-order structures (i.e., folds with a vertical axial plane), and (4) a tight syncline between the overturned limb and the autochthonous succession.

We performed a total number of 67 simulations varying mechanical and/or geometrical variables. During the early deformation stages, all the simulations share common features. With the onset of the shortening, the upper units (i.e., allochthonous nappes in Fig. 6) thicken, and the units below are increasingly buried as the simulation progress (Fig. 6A and B). The displacement of the upper nappes over the E-C unit and towards the foreland (i.e., left side of the simulation; Fig. 6E) usually reveals a low-angle, high strain-rate zone through the upper weak layer (i.e., the allochthonous Keuper). The E-C granite unit induces a strong mechanical heterogeneity in the shortening direction and triggers a concentration of the stress within the modelled Devonian and Upper Cretaceous layers near the contact between them (Fig. 6C). During these

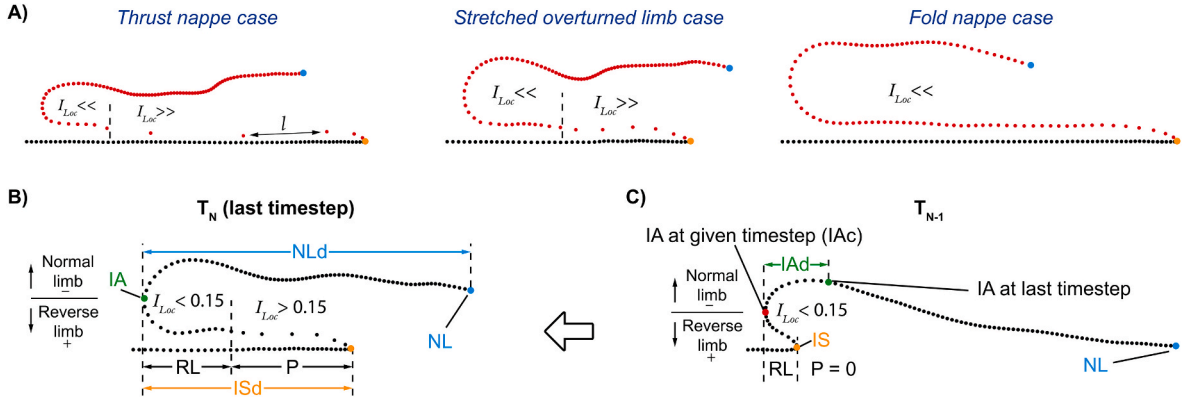

Fig. 5. A) Passive tracers extracted from the thrust nappe and fold nappe end-members and from an intermediate case between the two (stretched overturned limb). The longitude l between tracers is increasing from the fold nappe to the thrust nappe members as is the I_{Loc} parameter, which can be used as a tracker for quantifying the localisation. **B and C)** Quantification of the hinge migration for a fold nappe end-member by using passive tracers. Tracers in the normal limb are travelling towards the inflection point (IA) while the passive tracers in the reverse limb are moving away of it. The sign of tracers is changed as a function of their position in the reverse or the normal limb taking as a reference the tracer located in the hinge inflection of the fold (tracer IA).

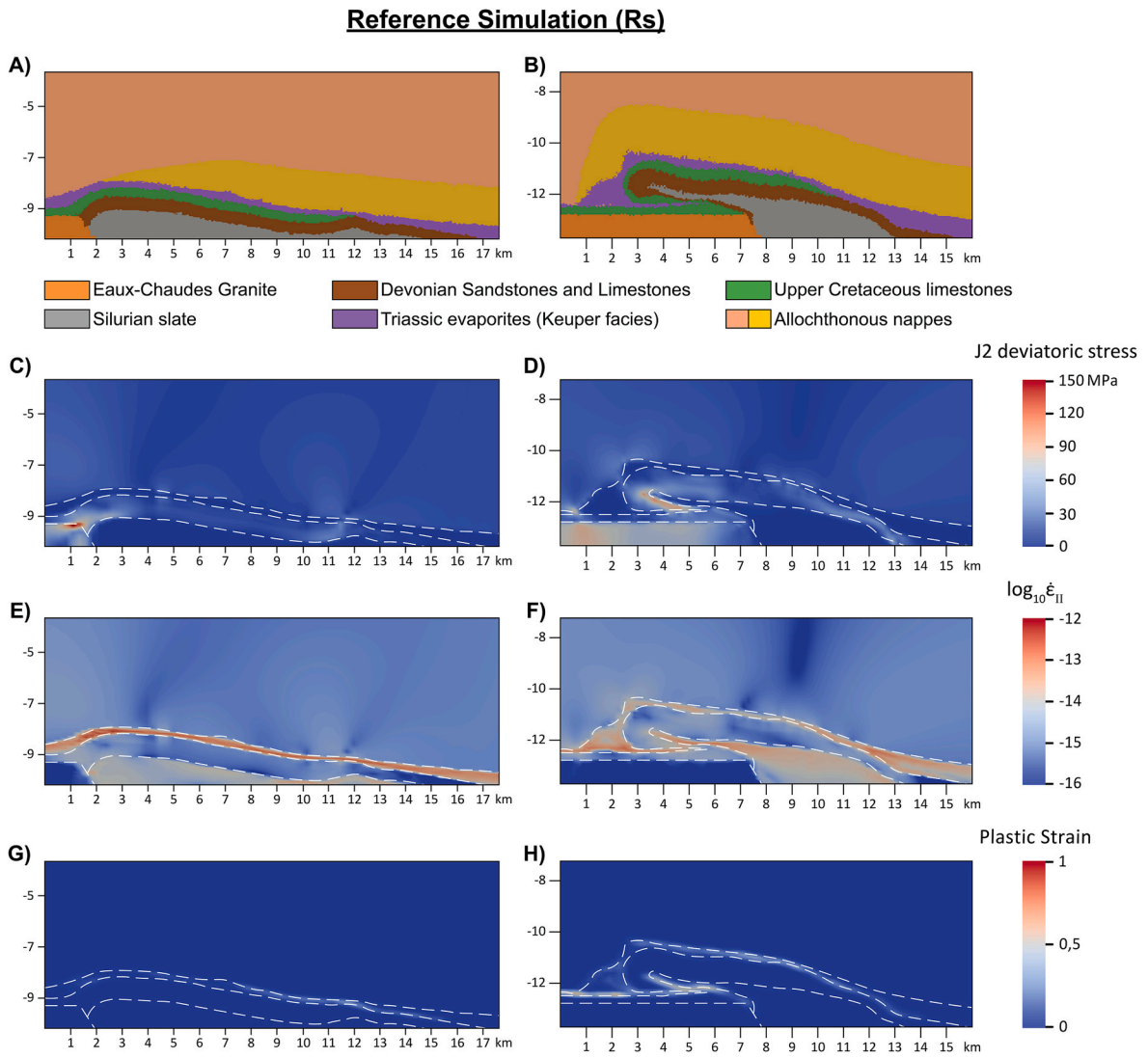

Fig. 6. A, B) Geometrical configuration after 22% (early stage) and 41.6% bulk shortening (late stage). **(C, E, G)** Variation of the deviatoric stress, the total second invariant of the strain-rate tensor ($\dot{\varepsilon}_{II}$ in log scale) and the accumulated plastic strain for 22% of bulk shortening. For this early stage, the maximum deviatoric stresses are observed in the footwall of the structure, and the maximum $\dot{\varepsilon}_{II}$ and plastic strain along the upper weak level. **D, F, H)** Plots of the deviatoric stress, the second invariant strain-rate and accumulated plastic strain for 41.6% bulk shortening. The maximum stresses occur in the overturned limb, the maximum strain rates in the lower weak level and at the top of the autochthonous footwall while the strain localisation in the upper weak level is partially deactivated, causing the coupling between the allochthonous and the lower E-C nappes. The accumulated plastic strain is observed mainly in the reverse limb and in front of the structure, with values relatively low to moderate compared to the bulk natural strain (i.e., the natural logarithm of the ratio between final and original length of the model) of approx. e = 0.89.

initial stages of shortening, the mechanical heterogeneity results in the nucleation and growth of a gentle, foreland-verging asymmetric fold. The vertical amplification of its frontal part results in the squeezing of the upper weak layer (Fig. 6A). The thinning of this layer reduces the efficiency of the decoupling in this upper localisation level at the base of the upper thrust sheets, indicated by a one-to-two order of magnitude drop in the second invariant of the strain rate (i.e., from 10^{-12}-10^{-13} 1/s to 10^{-14}-10^{-15} 1/s) until the end of the simulations. At the same time, a low-angle strain localisation zone becomes active within the lower weak unit (Fig. 6E and F). The supplementary material (Fig. SMM1-3) includes a movie with the temporal evolution of the geometry, the second invariant of the stress and strain rate tensors, and the plastic strain.

Supplementary video related to this article can be found at https://doi.org/10.1016/j.jsg.2024.105314

5.1. Reference model

The results of the reference simulation are presented in Fig. 6 after 22.7% (Fig. 6A) and 41.6% of bulk shortening (end of the simulation; Fig. 6B). By changing one variable or a combination of two variables (see Table 2), we performed the other simulations (Figs. 7–9).

The displacement of the allochthonous nappes over the E-C nappe enables an upper localisation level during the early stage of the simulation (Fig. 6E), and the stress concentration in the stiff basement area (Fig. 6C) causes the vertical amplification of the nappe, squeezing the upper weak layer and mechanically coupling the allochthonous nappes and the E-C nappe.

The reference model shows no general plastic yielding in the Upper Cretaceous unit (Fig. 6H). This lack of yielding led to an asymmetrical fold growth, where the dip of the reverse limb increased (until vertical) and later rotated towards the foreland. Amplification of the lower nappe drifts into nappe coupling and the activation of a lower detachment zone

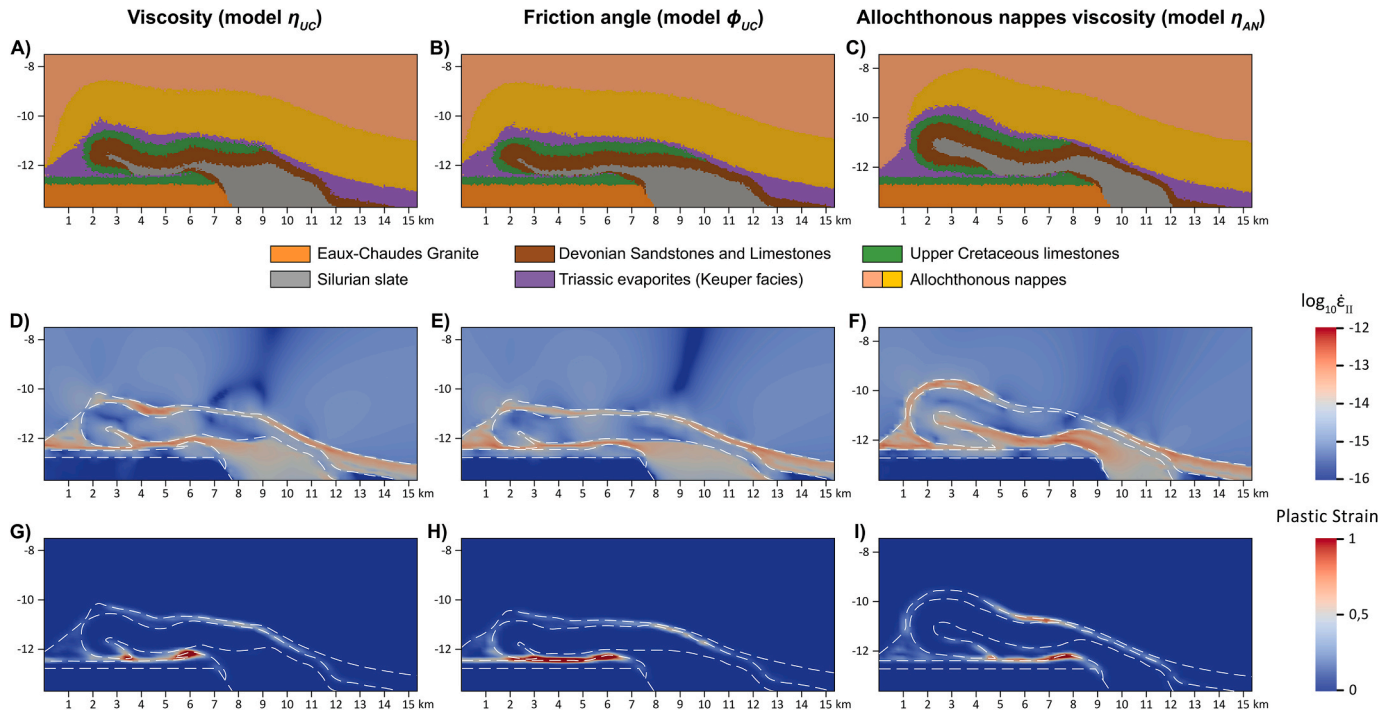

Fig. 7. Effect of the mechanical parameters tested (see text for explanation; the range of values is shown in Table 2). **A), D)** and **G)** Final geometry and distribution of the second invariant of the strain-rate tensor and plastic strain for a model with $\eta_{UC} = 10^{23}$ Pa s. **B), E)** and **H)** Geometry, second invariant of the strain-rate tensor and plastic strain plots for a model with $\phi_{UC} = 15^{\circ}$. **C), F)** and **I)** Geometry, second invariant of the strain-rate tensor and plastic strain plots for a model with $\eta_{AN} = 10^{22}$ Pa s, which enhances the brittle behaviour of the Upper Cretaceous level.

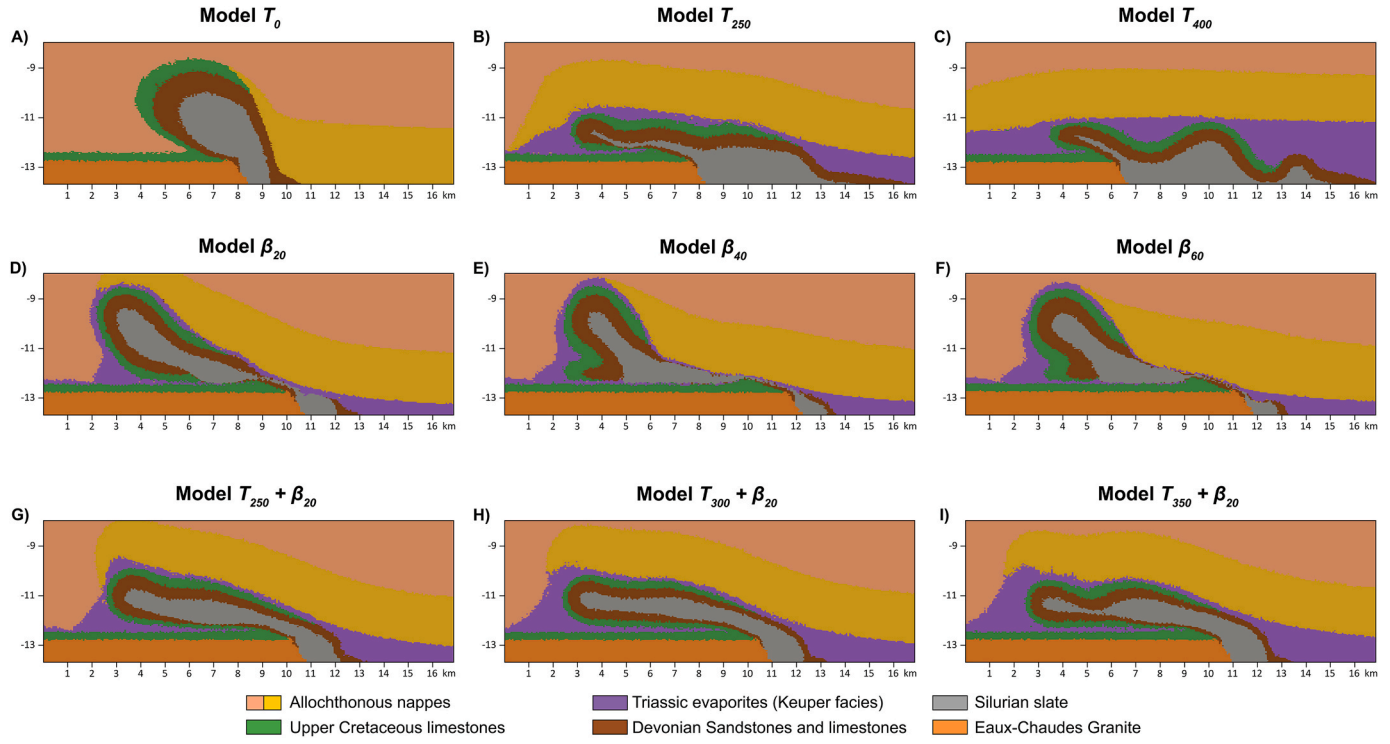

Fig. 8. Graphical summary of results exploring the effect of the geometrical variables. **A)** Thickness T = 0 m, **B)** T = 250 m, **C)** T = 400 m, **D)** Ramp angle $\beta = 20^{\circ}$, **E)** $\beta = 40^{\circ}$, **F)** $\beta = 60^{\circ}$, **G)** T = 250 m + $\beta = 20^{\circ}$, **H)** T = 300 m + $\beta = 20^{\circ}$ and **I)** T = 350 m + $\beta = 20^{\circ}$. Parameter values increase from left to right (see Table 2 for additional information).

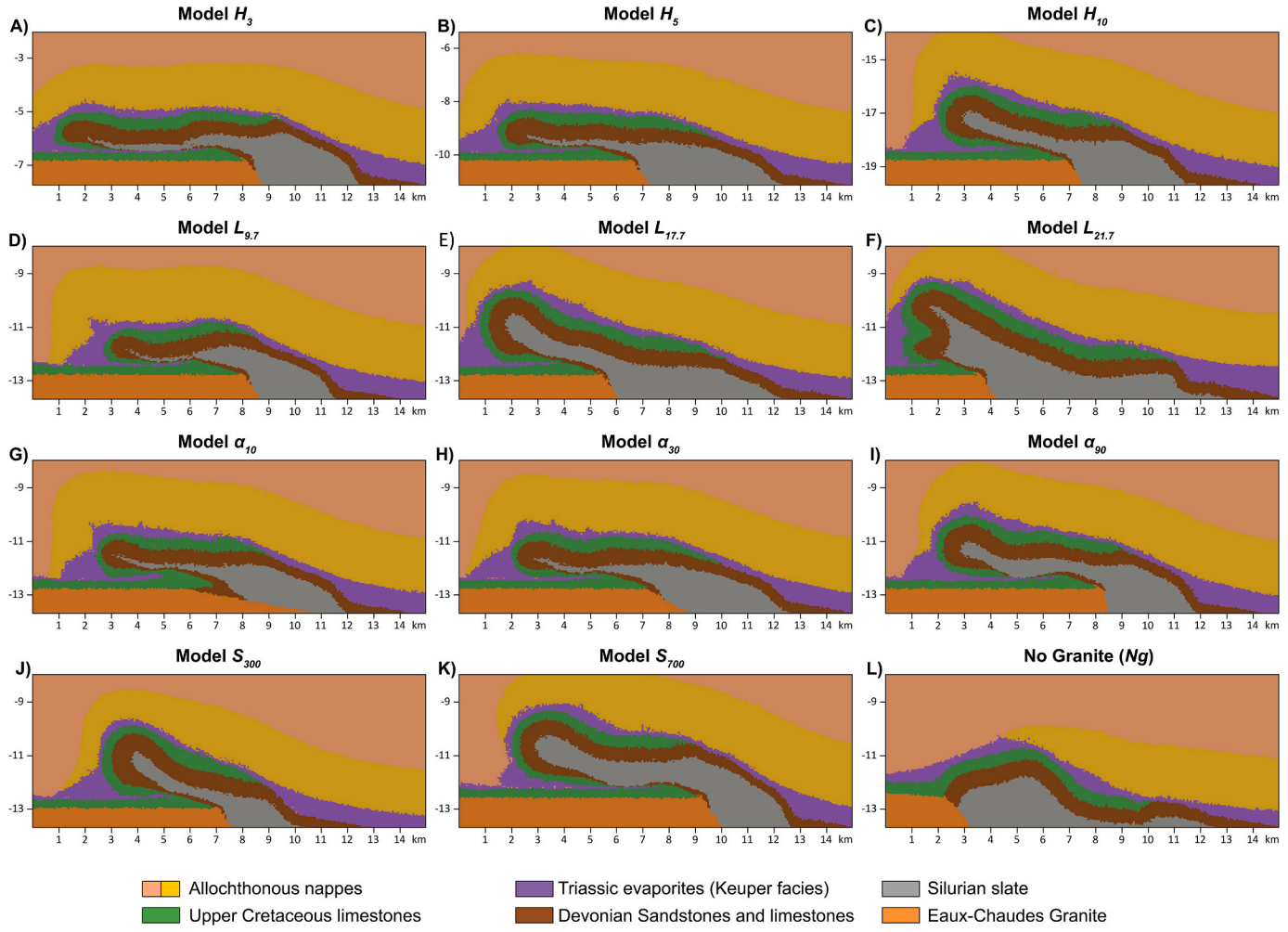

Fig. 9. Final geometry for models varying: **A-C)** the burial thickness (H), **D-F)** the initial length of Upper Cretaceous basin (L), **G-I)** the angle of the of the E-C footwall (α), **J-K)** the thickness of the Silurian weak layer and **L)** the absence of a strong forestop (or granite with similar properties than Devonian layer). Subindexes indicate the parameter values. (see Table 1 for additional information).

within the lower weak unit (i.e., Silurian slates; Fig. 6F). As the simulation progresses, the rotation of the reverse limb increases until it becomes sub-horizontal and completely overturned. The stiff basement units (dark brown; "Devonian sandstones and limestones" unit) and the reverse limb (Fig. 6D) now concentrate the larger differential stress. This leads to the rotation and overturning of the reverse limb, followed by its thinning and stretching (Fig. 6B).

At the late stages, the resulting structure (Fig. 6B) resembles a fold nappe structure with a sub-horizontal and thinned overturned limb and underlain by a tight synform where the upper weak layer has been nearly squeezed out between the synform limbs (similar to a welded contact). The geometry of the overturned limb appears continuous, but it exhibits strong thinning, and a high strain-rate zone is visible within it (Fig. 6F). All these observations qualitatively point to a change from dominantly viscous behaviour in the overturned limb during the early to mid-stages of the simulation (Fig. 6G) to an increased plasticity during the late stages (Fig. 6H).

5.2. Intrinsic mechanical controls on nappe development

To explore the influence of mechanical parameters on the development of fold/thrust nappes we carried out a series of simulations by (i) increasing the viscosity of the Upper Cretaceous layer (model η_{UC}; Fig. 7A–D and G), (ii) reducing the friction angle to 15° of the Upper Cretaceous (model ϕ_{UC}; Fig. 7B–E and H) and (iii) increasing the viscosity of the allochthonous nappes to 10^{22} Pa s (model η_{AN}; Fig. 7C–F and I).

In all these models (i.e., varying η_{UC}, η_{AN} and ϕ_{UC}), the upper weak layer (i.e., Keuper allochthon) almost squeezed out along the footwall ramp of the Lakora thrust (Fig. 7A–C). The reduction of the thickness of the upper weak layer enhances the coupling between the E-C nappe and the upper allochthonous nappes, reducing the transport of the latter and facilitating the decoupling in the lower weak layer (i.e., the Silurian unit). This is documented by drops of the second invariant of the strain rate tensor within the upper weak layer with shortening, which points to the solidary translation of both units (Fig. 7D–F).

The results of the simulations increasing η_{UC} or decreasing ϕ_{UC} are very similar, and there is a positive enhancement of the brittle/plastic over the viscous/ductile behaviour of the Upper Cretaceous layer, especially for $\phi_{UC} = 15°$ (Fig. 7E and H). When compared to the reference simulation, both cases show a loss of continuity in the Upper Cretaceous unit. This loss occurs over a thin and localized level, marked by high strain rate values (10^{-13}-10^{-12} s^{-1}). This level cross-cuts the reverse limb of the structure, as shown in Fig. 7D and E. The E-C nappe is transported over this level without changing the length of neither the reverse nor the normal limb, and qualitatively pointing to an absence of anticline hinge migration after yielding. The resulting structure shows a relatively short, overturned limb with a gently-to-moderately dipping axial plane, being akin to a cut-off hanging wall anticline as in standard thrust tectonics (Fig. 7A and B).

As the viscosity of the allochthonous nappes increases, it also amplifies the (frictional) plasticity that affects the E-C nappe. However, this increase is minor compared to the previous η_{UC} or ϕ_{UC} variables (Fig. 7G–I). Shearing of the Upper Cretaceous is also observed, and the E-C nappe is then transported over a thin strain-localized level, also cross-cutting the reverse limb (Fig. 7F and I). The structure developed is thicker and possesses a larger overturned limb than those for variables η_{UC} and ϕ_{UC}, probably induced by a major extrusion and migration of the Silurian-analogue weak material towards the core of the anticline.

5.3. Geometrical controls on nappe development

We performed a second series of model runs to test the impact of the initial configuration of the mechanical units (dimensions, angles, burial, etc.) on the results. The geometrical variables tested are listed in Table 2, and the results are presented in Figs. 8 and 9. Briefly, we tested the following variables: 1) the thickness of the upper weak layer (T; series of models $T_{0\text{-}400}$), 2) the angle of the Lakora ramp (β; series of models $\beta_{20\text{-}90}$), 3) thickness and ramp angle combined (T+β; series of models $T_{250\text{-}400}$+$\beta_{20\text{-}40}$), 4) the depth of burial (H; series of models $H_{3\text{-}10}$), 5) the length of the Upper Cretaceous panel (L; series of models $L_{9.7\text{-}21.7}$), 6) the angle of the strong granite forestop (α; series of models $\alpha_{10\text{-}90}$) and 7) the thickness of the lower weak detachment layer (S; series of models $S_{300\text{-}700}$). In addition, the potential effect of lacking a strong mechanical unit, similar to the natural case east of the E-C granite (*Ng*; model No Granite), also underwent evaluation.

Increasing the thickness of the upper weak layer (models $T_{0\text{-}400}$; Fig. 8A–C) promotes a major displacement of the upper allochthonous units over the E-C nappe due to an enhanced decoupling. During displacement, there is a reduction of the shear transmission downwards, but it is not completely prevented. This is manifest from the limited progress of the E-C nappe towards the foreland margin of the simulation (Fig. 8A–C). This reduction of shear transmission hampers the activation of the lower weak level and prevents an efficient detachment and amplification of the frontal part of the nappe. In summary, the allochthonous thrust sheets and the E-C nappe are not coupled, and the displacement of the latter is inhibited, resulting in a geometry consisting of a fold with a short reverse limb and moderately dipping axial plane. Finally, the nappe shows additional large-scale secondary upright folds. For the case of a model without an upper weak layer (model T_0; Fig. 8A), neither a thrust nor a fold nappe develops, and instead a long-wavelength anticline with marked layer thickening forms. The lower weak layer then extrudes toward the core of the fold.

For an initial setting with the Lakora footwall ramp angle larger than the reference model (i.e., $\beta > 10^\circ$, but keeping T invariant) (model *Rs*; Fig. 6), larger strains are concentrated along the footwall ramp, promoting 1) stretching, thinning and segmentation of the Devonian layer along the normal limb, 2) shear localisation in the reverse limb, affecting Upper Cretaceous and Devonian units, and enhanced plastic deformation (Fig. 8D–F), and 3) thinning-out of the upper weak layer. Geometrically, the latter results lead to the "welding" of the thrust contacts between the E-C and upper nappes.

Increasing the β value (Fig. 8D–F) enhances the stress transmission normal to the Lakora footwall ramp which hinders the displacement of the upper nappes over the E-C nappe towards the foreland, promoting the early coupling of both structural units due to the squeezing of the upper weak layer over the footwall ramp area. It also causes the early activation of the lower shear zone through the lower weak unit. The Upper Cretaceous and the Devonian layers are lifted vertically near the Lakora footwall ramp and also on the strong granite area, and a large amplitude, km-scale upright fold is then developed. The early coupling makes the E-C nappe layers shear off, leading to a larger displacement of the E-C nappe over a thin and localized surface on top of the autochthonous units (Fig. 8E and F).

However, for the model with $\beta = 20^\circ$ (model β_{20}; Fig. 8D), longer overturned limbs are promoted compared to the reference model. The overturned limb of the structure is very gently-dipping forming a low angle with the autochthonous footwall.

Simulations combining increased thickness and ramp angle (i.e., variables T+β combined; models $T_{250\text{-}400}$+$\beta_{20\text{-}60}$; Fig. 8G–I and SMI1) produce final geometries with large and sub-horizontal overturned limbs and axial planes, favouring fold nappe development. In general, the increase in β enhances the efficiency of the stress transmission and the displacement of the allochthonous units towards the E-C nappe (Fig. 8G–I and SMI1). This is a remarkable difference from the series of models $T_{250\text{-}400}$ and $\beta = 10$, which did not reproduce large, sub-horizontal overturned limbs and axial planes (Fig. 8A–C). The increase to 20° promotes the activation of the lower shear zone within the lower weak Silurian layer, without the shearing off the E-C nappe forelimb as happens when T is < 250 m (Fig. 8D), and this results in a large and sub-horizontal reverse limb (Fig. 2B and 8G-I).

As in the series of models $\beta_{20\text{-}90}$, in the performed simulations with $\beta > 20^\circ$ (provided in the supplementary material), both the Upper Cretaceous and Devonian layers show thinning and boudinage in the overturned limb, and in the Devonian of the normal limb, and the structure is resolved in a thin strain-localized level (also affecting the Devonian of the normal limb) that controls the structural transport (Fig. SMI1).

In these combined T+β simulations, the existence of a thicker weak Keuper layer ($T > 250$ *m;* Fig. 8G and H) promotes the decoupling between the upper allochthonous and the lower E-C nappes. This leads to the formation of horizontal axial planes and fold nappe overturning due to the high capacity to flow of this low-viscosity layer. This layer can be extruded from the footwall syncline (Fig. 8H). For these simulations (i.e., $\beta = 20^\circ$ and $T > 250$ m), the overturned limbs fairly maintain the thickness of the Upper Cretaceous layer, although a bit of thinning is observed near the footwall syncline, especially for simulations where the upper weak layer is thinner than the reference model (Fig. 8G). When $T \geq 350$ m (maintaining $\beta = 20^\circ$) secondary gentle folds form in the normal limb (Fig. 8H and I).

For this succession of models changing variables *T and* β, the thickness of the overturned limb does not change substantially during deformation, which points to a potential mechanism of hinge migration and rigid rotation of the overturned limb, instead of limb stretching and shearing. In any case, the geometries obtained in models with T+β indicate dominantly viscous rather than plastic behaviour.

Varying the burial depth (series of models $H_{3\text{-}10}$; Fig. 9A–C) leads to a significant variation of the structural results. The simulation with an initial $H < 5$ km (shallower conditions; Fig. 9A) results in the cut-off of the Upper Cretaceous short reverse limbs, producing thrust ramp anticlines. Thrust nappes displace over a localized detachment located in the Silurian weak level, as observed in prior η_{UC} and ϕ_{UC} simulations (Fig. 7A and B). The UC layers maintain their original thickness (Fig. 9A), even with thinning in the reverse limb of the structure, which points to a dominantly plastic/frictional behaviour.

Conversely, for $H > 5$ km the resulting structures always have a continuous overturned limb. Higher burial favours the conservation of the thickness of the UC layer and larger overturned limbs, pointing to a dominantly viscous behaviour of the Upper Cretaceous layer (Fig. 9B and C).

For a series of models varying the initial length of the UC layer (L), shorter layer lengths produce structures resembling thrust nappes (models $L_{9.7\text{-}21.7}$; Fig. 9D). On the other hand, larger original layers (Fig. 9E and F) increase the dip of the structural elements (i.e., reverse and normal limbs and fold axial plane) towards the hinterland. In addition, for such cases the reverse limb of the structure is also relatively short, and the Silurian weak level is thickened in the core of the fold (Fig. 9E). Furthermore, for $L > 17.7$ km, secondary folds appear in the hinge and normal limb leading to an increase in the structural relief of the E-C nappe.

The contact angle between the granite and stiff autochthonous E-C footwall (model $\alpha_{10\text{-}90}$; Fig. 9G–I) is also relevant. For $\alpha \leq 60^\circ$ (model *Rs*;

Figs. 6 and 9G and H), the simulated nappes show a thinned and stretched reverse limb. On the other hand, when $\alpha = 90°$ (Fig. 9I) early coupling between the upper allochthonous nappes and the E-C nappe occurs due to the amplification of an upright fold in the contact between stiff granite and lower detachment layer level. The high α angle causes the weaker level to extrude. The E-C nappe is sandwiched in between the push of the upper nappes and the granite, shearing off the Devonian and Upper Cretaceous layers in the forelimb (Fig. 9I). Fig. 9J and K displays the results of models that vary the initial thickness of the lower weak layer, simulating the Silurian in the natural case (simulations S_{300} and S_{700}). For S_{300} model, with a thickness lower than the reference model, the E-C nappe panel shows less advance towards the foreland than the reference model. Activation of the Silurian detachment occurred only at the late steps of the simulations due to the absence of nappe coupling until that point. This results in a fold with a short reverse limb, with thickness constant due to the limb rotation (Fig. 9J). On the contrary, an increase of the lower weak thickness (model S_{700}; Fig. 9K) results in longer reverse limbs and shearing off the Upper Cretaceous and Devonian layers. Furthermore, the weak layer is thickened in the fold cores, which results in an increase of the structural relief.

Finally, the absence of the strong footwall body, which in this simulation was replaced by a deformable basement with mechanical properties similar to the Devonian (model *Ng*; Fig. 9L), produces the development of large-scale upright buckle folds and prevented the development of thrust/fold nappes. This highlights the importance of a strong footwall unit in the development of fold nappe structures.

6. Synthesis and discussion

For a more quantitative analysis of the structural transition between fold and thrust nappes, we analysed and categorized the modelling results using various geometrical and mechanical variables.

6.1. Quantification of the strain localisation factor (I_{Loc})

We used the UC layer to constrain the evolution of the degree of strain localisation (I_{Loc}; see methodology section). In the current simulations, the region expected to acquire the higher strain localisation is the overturned limb, and hence, the I_{Loc} factor permits to quantitatively discriminate between cases with uniform thickness (low I_{Loc} values) from cases with strongly heterogeneous thinning of the overturned limb (I_{Loc} near 1).

Fig. 10 displays the results of the analysis for a series of selected models (Fig. 10A) and all simulations (Fig. 10B). The general trend of the I_{loc} is to increase with time. The data reveal three basic evolution patterns:

1) Simulations that evolve with a fast increase of I_{Loc} up to stabilisation at high values ($I_{Loc} > 0.7$). Models with a tendency towards thrusting, with high accumulated plastic strain and strong shearing and thinning of the reverse fold limb, display this trend. Examples of this type are the simulations with low initial burial (e.g., H_3; Fig. 9A), high viscosity of the allochthonous nappes (e.g., η_{AN}; Fig. 7C), low frictional angles (e.g., ϕ_{UC}; Fig. 7B) or moderate to short dimension of the UC panel (e.g., $L_{9.7}$; Fig. 9D). This type corresponds to the category labelled as "thrust nappes" (Fig. 10A).
2) Simulations with a flat distribution in time and low values of I_{Loc} (<0.15). This type corresponds to models displaying fold nappe geometries, with the Upper Cretaceous level keeping a homogenous thickness without low stretching, and overall dominated by viscous flow. There are few simulations displaying this trend (Fig. 10B), but examples are those characterized by a thick initial upper weak layer (e.g., model $T_{300} + \beta_{20}$; Figs. 8H and 10A). This type corresponds to the category labelled as "fold nappes".
3) Simulations with an initial flat trend but displaying a moderate increase of the I_{Loc} after some deformation. This type corresponds to simulations resulting in hybrid geometries between fold and thrust nappes, showing gradual stretching and thinning of the overturned limb, without losing its continuity, and low plastic deformation. Most of the models performed correspond to this type, such as the reference simulation (e.g., *Rs* model; Figs. 6 and 10A). This type corresponds to the category labelled as "fold nappes with stretched recumbent limb".

An attempt to define the boundaries between these three main categories was calibrated using as a reference the last step of the simulations, in which the amount of shortening is maximum. The first category labelled as "fold nappe" was defined when $I_{Loc} < 0.15$ and corresponds to idealized fold nappes in which the thickness of the overturned limb is constant, the stretching of the overturned limb is relatively low, and the

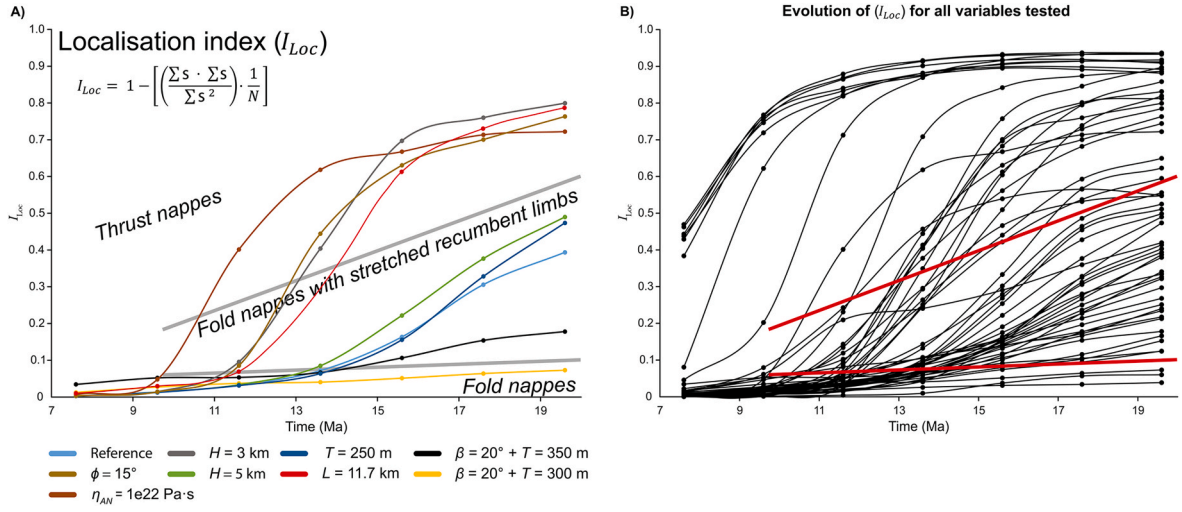

Fig. 10. A) Evolution of the localisation index I_{Loc} with respect to the simulation time for the reference simulation and for selected parameters varied from it as shown in Tables 1 and 2 This diagram illustrates the recumbent fold nappe (β = 20° + T = 300) and the thrust nappe (H = 3 km) end-members. Thrust nappes exhibit a fast rise of the index and fold nappes show low and stable behaviour of the index through time. Fold nappes with stretched reverse limb possess features from fold nappes (initial stable slope) and thrust nappes (moderate rise), attesting for the limb stretching. **B)** Evolution of the I_{Loc} with time plotted for all simulations undistinguished. The most frequent trends correspond to "thrust nappes" and "fold nappes with stretched limb", and only in three cases we observe homogenous thickness and little localisation corresponding to the "fold nappe" case.

deformation was accommodated in a dominant viscous behaviour; a second type labelled as "fold nappes with stretched reverse limb" alludes to fold nappes with I_{Loc} between 0.15 and 0.6, where the overturned limb is continuous but shows moderately to strong thinning and stretching; and finally, a third type represents $I_{Loc} > 0.6$ and makes reference to thrust nappes, where the reverse limb is not continuous between both walls and the dominant behaviour is plastic (Fig. 10). Because there is a general tendency to increase I_{Loc} with time, these boundaries cannot be defined as a strictly straight line in the diagram and were defined using a positive slope.

6.2. Quantification of the fold hinge migration

A passive tracer grid predefined in the UC unit served as the tool for assessing fold hinge migration during deformation (Fig. 4A and 5). This mechanism accounts for the observation of long recumbent limbs with preserved thicknesses, a feature that is in general difficult to explain by a fixed-hinge mechanism and limb stretching (Fig. 11). For more detailed explanation, see methodology section.

Fig. 12 illustrates several examples of the evolution of hinge migration in the framework of the three main categories distinguished by the localisation index (Fig. 10A). For the case of the "thrust nappe" category (e.g., model H_3; Fig. 9A), the IA tracer trajectory (green curve) migrates during the early stages of fold growth, but it quickly becomes fixed to the material particles (approx. 11.0 Ma), up to the end of the simulations (Fig. 12A). This indicates that in this category, the hinge of the fold is blocked and cannot migrate (e.g., Fig. 11). On one hand, the normal limb NL always shows a positive tendency with time, with a reduction of its distance with respect to the IA and thus indicating that part of the deformation was accommodated by the progressive shortening of the normal limb. On the other hand, the IS during the early stages was located relatively near the IA, but relatively soon in the model run (approx. 9.2 Ma) the relative distance between both markers started to increase. An analysis using the $I_{Loc} > 0.15$ condition shows that the major increase in distance is due to plastic deformation (P) and the length of the "low deformed" reverse limb was relatively short and constant during all time.

For the case of the "fold nappe" category (e.g., model $T_{300} + \beta_{20}$; Fig. 8H), the trajectory of the IA tracer describes a continuous positive tendency, with displacement of the material particle from the normal limb towards the inflection point (reached in the last step by the definition of the IA). The NL and IS curves show also a similar trend, with a tendency to increase their relative distances respect to the IA (Figs. 11 and 12B). The strain localisation analysis indicates that the I_{Loc} threshold remains not exceeded (i.e., $I_{Loc} > 0.15$). Therefore, distributed viscous flow mainly accommodated the deformation (very low plastic deformation). For the example shown in Fig. 12B, there was a migration of the hinge equivalent to 4 km.

Finally, for the case of "fold nappe with stretched reverse limb" category (e.g., *Rs* model; Fig. 6), the IA, NL and IS trajectories show trends between the previous two cases. The IA displays a large interval of time with hinge migration until approx. 17.7 Ma of simulation time, when it became fixed and remained until the end of the simulation (Figs. 11 and 12C). Pre-stage before blocking of the fold hinge causes the I_{Loc} to rise over 0.15 (approx. 13.7 Ma), resulting in the stretching of the reverse limb by viscous and plastic flow until the end of the simulation.

Therefore, the numerical modelling presented here indicates that the migration of the fold hinge is a plausible mechanism in recumbent folding and contributes to preserve the thickness of the recumbent limbs (e.g., Figs. 11, 12B and C).

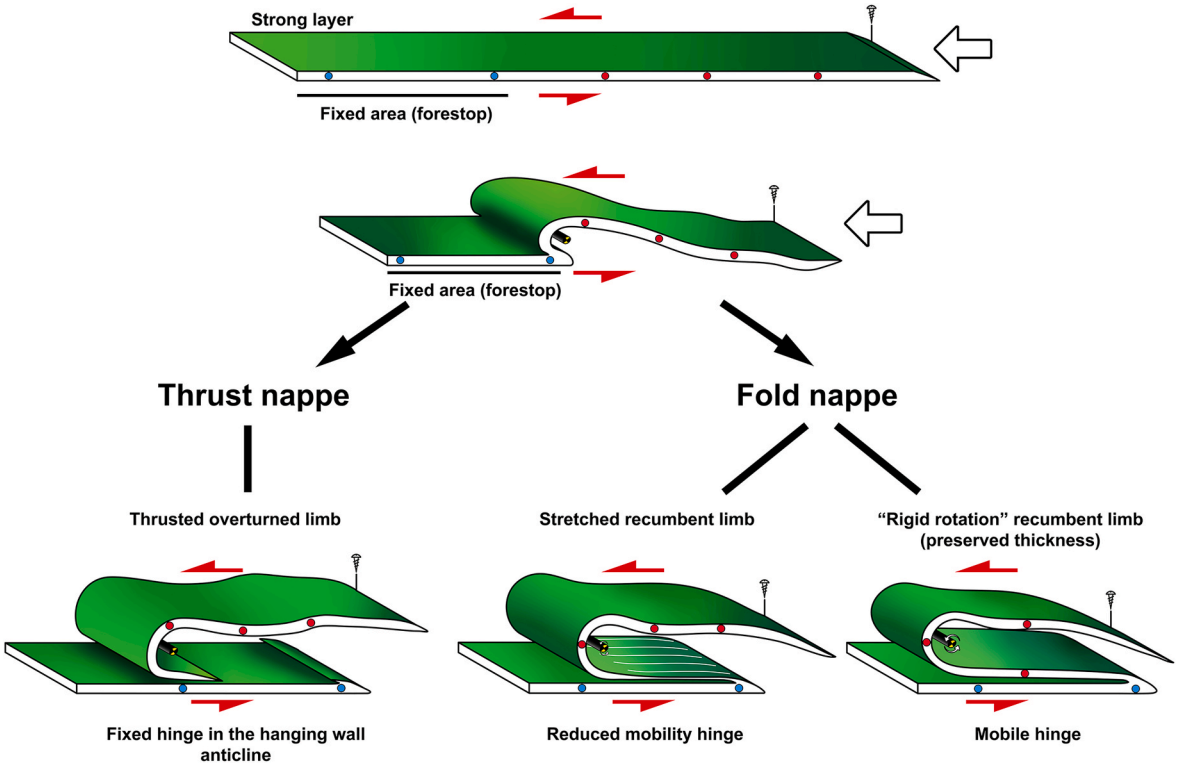

Fig. 11. Sketch of the principal mechanisms under which the thrust and fold nappe end-members may evolve from an initial flat layer. A sedimentary panel with a fixed area (blue dots) is subjected to layer-parallel compression and shear is developed above and below the panel. The fixed area acts as a buttress, first nucleating a buckling anticline, and the structure is then translated to the foreland. Progressive deformation can lead to an idealized thrust nappe (blocked hinge) or to an idealized recumbent fold nappe, in which the thickness of the recumbent limb is preserved (mobile hinge). Mobility of the hinge is defined by the transport of the material particles (red dots) through the different structural elements. Between both end-members, a potential type is defined by the stretching of the recumbent limb and less efficient migration of the fold hinge. (For interpretation of the references to colour in this figure legend, the reader is referred to the Web version of this article.)

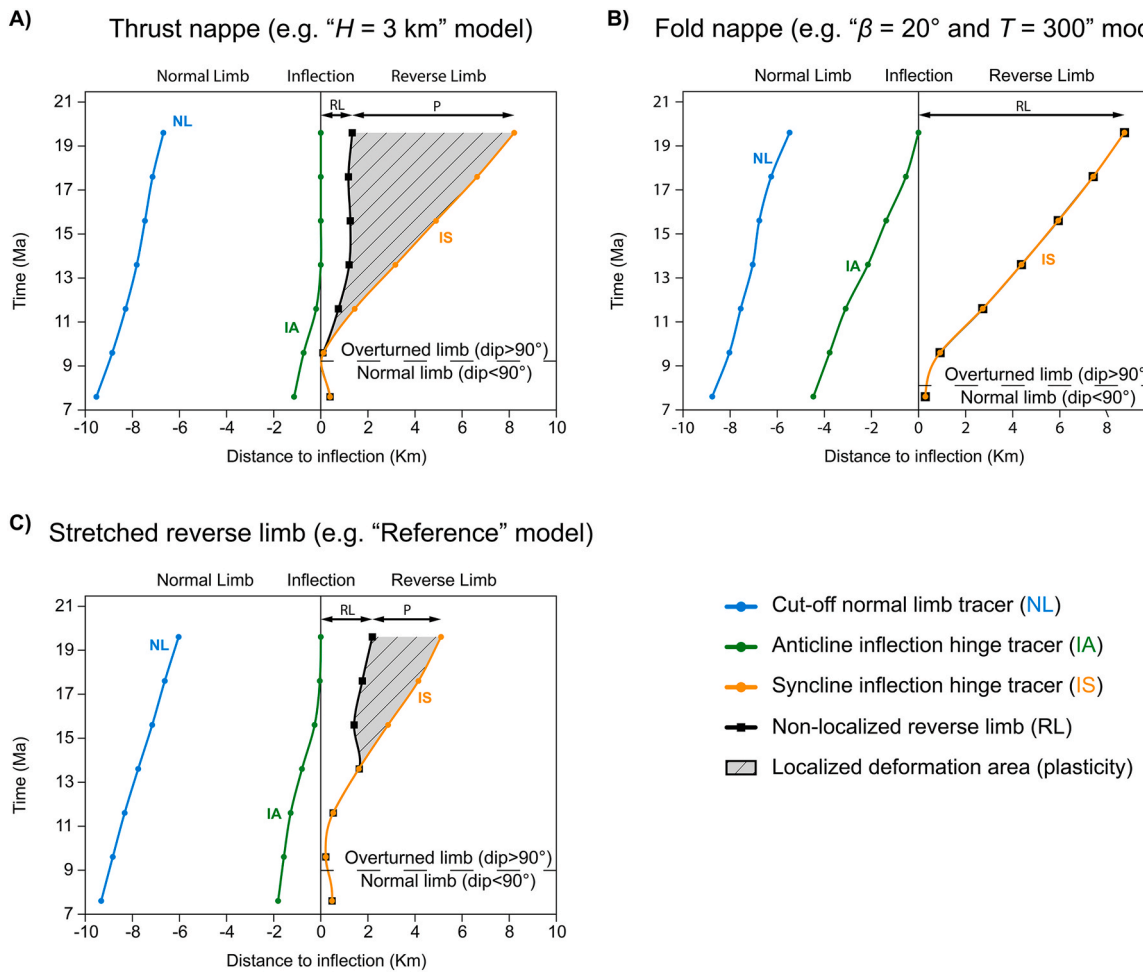

Fig. 12. Plot of the variation of the position of the three passive tracers with respect to the fold inflection. **A)** Thrust nappe end-member, where the hinge migration is locked from 13 Ma onwards and the plasticity (P) is increasing ($I_{Loc} > 0.15$) from the early simulation time, causing an extreme stretching and thrusting of the reverse limb at the end. **B)** Fold nappe end-member; hinge migration is active until the end of the simulation and there is no plasticity in the reverse limb (P = 0 and $I_{Loc} < 0.15$). **C)** Stretched reverse limb case ($0.15 < I_{Loc} < 0.6$), showing mixed features between the fold nappe and thrust nappe end-members, where the migration of the hinge is active until 13Myr and then it is inhibited, which results in the stretching of the reverse limb.

6.3. On the influence of geometrical and mechanical variables in the nappe geometry

Fig. 13 summarizes the effect of changing the different variables on the I_{loc} parameter (Fig. 4; Tables 1 and 2). The diagram is divided into the three defined categories: thrust nappes, fold nappes with stretched reverse limb and fold nappes. The red points indicate the reference simulation.

On one hand, from Fig. 13, thrust nappe geometries are sighted when there is an increase of mechanical variables such as the viscosity of the upper allochthonous nappes (η_{AN}) or the viscosity of the Upper Cretaceous (η_{UC}), or when there is a decrease of the frictional angle of the Upper Cretaceous layer (ϕ_{UC}). The geometrical variables that promote thrust nappes are short L and H, thin detachment levels (T), and, in general, moderate/large angles of the Lakora ramp (β) or the forestop (α). On the other hand, the variables promoting fold nappes preserving layer thickness are very restricted. The systematic series of models reveal a positive enhancement of fold nappe occurrence only for moderate values of viscosity of the upper allochthonous nappes (η_{AN}) or with an increase in the thickness of the upper detachment level (T). In general, the most likely situation in the series of performed models is the development of fold nappes with stretched limbs and very heterogenous strain distribution.

From a kinematic and mechanical perspective, the development of thrust vs. fold nappes is relevant for the spatial distribution of stress and strain rate (Fig. 14). In synthesis, common features of all the simulations showing a thrust-nappe result are the development of a high-strain deformation band cross-cutting through the Upper Cretaceous layer (e.g., Figs. 14A and E or 7D-F) and the accumulation of elevated plastic strain in the reverse limb (e.g., Figs. 7G–I and 14G), indicating predominant plastic-brittle conditions. From a geometrical point of view, this causes the development of short or very short reverse limbs in hanging-wall anticlines, and overall low structural relief. As for the localisation index, the process is characterised by a "fast" increase of the I_{Loc}, passing from conditions of distributed strain (low I_{Loc}) to moderate/high values > 0.4–0.6 in a short time. Additionally, this is also coincident with the blocking of the fold hinge migration which enhances the early plastic yield of the material and the extreme stretching of the overturned limb (Figs. 10A, 11 and 12). The spatial transition from little deformed to highly deformed is rapid (e.g., Figs. 7B and 12A).

On the other hand, continuity of the reverse limbs and moderate structural relief characterize the fold nappe end member (Fig. 14B). In contrast to thrust nappes, plastic strain is very low, stress and strain rates are moderate/low, and high strain zones cross-cutting the overturned limb are not formed (Figs. 12B and 14F and H). The fold nappes exhibit km-scale overturned limbs without significant heterogeneous stretching and strain localisation (e.g., Fig. 11), and dominated by viscous flow (I_{Loc} <0.15; Figs. 10A and 12B). However, it is essential to consider this

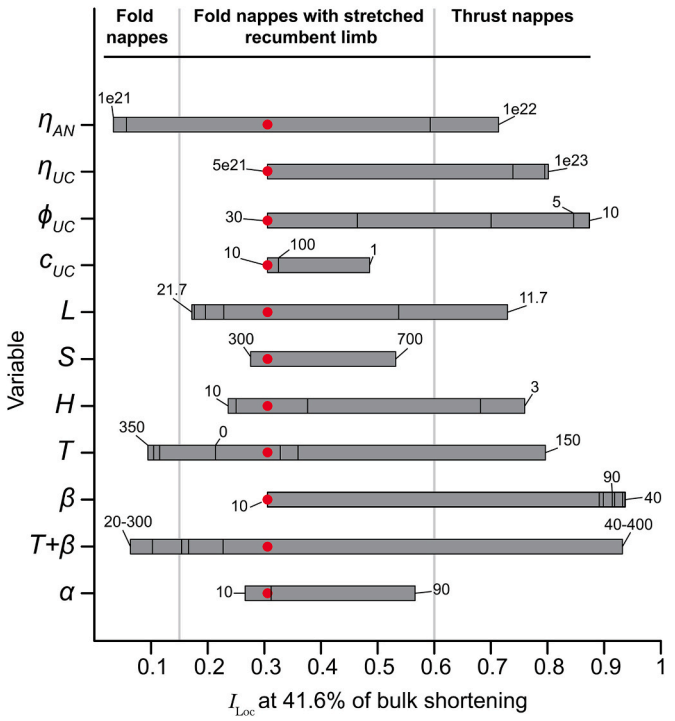

Fig. 13. Range of variation of the index of localisation for each variable tested and structural style developed. The red point indicates the reference simulation, while numbers indicate the range of values used for each variable. (For interpretation of the references to colour in this figure legend, the reader is referred to the Web version of this article.)

end member as an idealized or very restrictive structure, and probably the more usual cases in nature are with $I_{Loc} > 0.15$ with stretched overturned limbs (Figs. 10B and 11).

Figs. 8G and I and 9B present more realistic recumbent folds, where the reverse limbs are stretched, but without attaining the plastic yielding during the early/intermediate stages of deformation. Accordingly, the I_{Loc}, never overcomes the thrusting boundary (Fig. 10A). Overturned limbs show continuous thinning, and they can achieve plastic yield during the last stages, producing the progressive localisation of deformation. Such localisation may represent the basal thrust observed in some natural fold nappes. The resulting structures show many of the first-order features observed in natural examples (i.e., a flat-lying reverse limb of kilometric scale, a normal limb with second-order structures, a sub-horizontal axial plane and a tight syncline between the recumbent limb and an autochthonous succession), as in the Helvetic nappes of the Swiss Alps (e.g., Ramsay et al., 1983; Pfiffner, 1993).

6.4. *Application to the Eaux-Chaudes fold nappe and comparison with other cases*

Our modelling results highlight the important mechanical and geometrical controls by the mechanical stratigraphy and the tectonic inheritance, features that we interpret played a fundamental role in the development of the Eaux Chaudes fold nappe during the Alpine deformation of the Pyrenean hinterland. For this specific natural case, two main factors arise as first-order controls: (1) the presence of a stiff forestop in the shortening direction to produce a buttress condition (i.e., the Eaux-Chaudes granite), and (2) the existence of two weak layers (i.e., the Keuper and the Silurian) that favoured the structural decoupling and localisation of the deformation.

Based on previous numerical models applied to the Helvetic Alps by Kiss et al. (2020) and Spitz et al. (2020), the development of nappe structures with large-scale stratigraphic overturning or/and displacement requires a viscosity contrast of about three orders of magnitude between the strong key levels and the upper and lower weak detachment levels. In situations with lower viscosity contrast or without an upper weak level, fold nappe structures with large displacement did not form (e.g., Fig. 8A).

The numerical simulations presented here show that tectonic inheritance in the form of a basement forestop controls the nappe initiation by concentrating stress in the contact between the strong layers (immersed between weak layers) and the forestop (Fig. 6C). Similar results have been obtained by Bauville and Schmalholz (2017), Kiss et al. (2020), and Spitz et al. (2020) in simulating the Helvetic nappes, which indicates to a common mechanism of nappe initiation. If the mechanical heterogeneity of the viscous contrast between the simulated granitic and metasedimentary basement was absent (Fig. 9L), neither a fold nor a thrust nappe was produced, but large-scale upright buckle folds formed instead. The push and shear stress provided by the Lakora thrust and the upper allochthonous nappes (e.g., the Ultrahelvetic nappes in the case of the Alps) concentrated the stress along the contact between the E-C pluton and the Upper Cretaceous limestone interface, as suggested by the reference simulation (Fig. 6C). This led to the activation of the Silurian lower detachment of the E-C nappe and the growth of the structure. Hence, the Eaux-Chaudes pluton (with apparently no signs of significant ductile deformation during the Alpine compression) played an essential role for recumbent folding. This example highlights the role of tectonic inheritance and mechanical heterogeneities arising from pre-alpine rocks during the Pyrenean orogeny, such as also documented for the Alps (e.g., Wissing and Pfiffner, 2003; Kiss et al., 2020). However, in contrast to the Helvetic nappes of the Alps, in the case of the Eaux-Chaudes massif we cannot invoke the ductile closure of precursor extensional basins and the extrusion of their sedimentary infill. Indeed, the results indicate that mechanically developing a fold nappe requires a minimum initial burial condition of ~5 km in depth (Fig. 9A–C), which is in accordance with the proposal by Caldera et al. (2021) of emplacement conditions under 8–10 km of rock. Our results also emphasize the role of the upper Keuper allochthonous weak layer, enabling the decoupling between structures but also allowing the growth of the recumbent fold given its capacity to flow and migrate.

The multilayered character of the models with weak rocks such as slates, shales or evaporites between stiffer layers triggered the development of the upper and lower shear zones (Fig. 6E and F) that are necessary for the development of the fold nappe structure. In addition, model set ups with a thicker upper detachment level (T ~250–350 m) favour the development of recumbent fold structures because they allow the decoupling from the allochthonous upper nappes since the early steps of the convergence (e.g., Fig. 6E). However, for settings with very large thickness of the upper weak layer the shear stress transmission downwards becomes less efficient and may inhibit the activation of the Silurian basal detachment (for $T > 350$ m; Fig. 8C). On the other hand, an excessive thinning of the upper weak layer reduces the efficiency of decoupling between this weak layer and the E-C nappe (e.g., Fig. 8F) positively enhancing the shear transmission downwards, and causing that the low angle shear zone within the lower weak level becomes the only active level until the end of the simulation (Fig. 6E and F). Pfiffner (1993) made similar observations, where high ratios between the thickness of the weak to the stiff layers favoured the development of fold nappes. From a qualitative interpretation based on the final geometry, the simulations with I_{Loc} displaying moderate to low values ($\ll$0.6 Figs. 8G–I, 10A and 12B) are the cases that most closely resemble to the E-C natural example.

Furthermore, the cases where 1) the upper allochthonous nappes and the E-C nappe are relatively coupled and 2) the lower shear zone is active, are the optimum situations for the mechanism of fold hinge migration and limb rotation (and unfolding?) as ways to overturn the forelimb during the early deformation steps. Even though both amplification mechanisms by limb stretching and hinge migration coexist in all our simulations, geometries approaching recumbent fold nappes

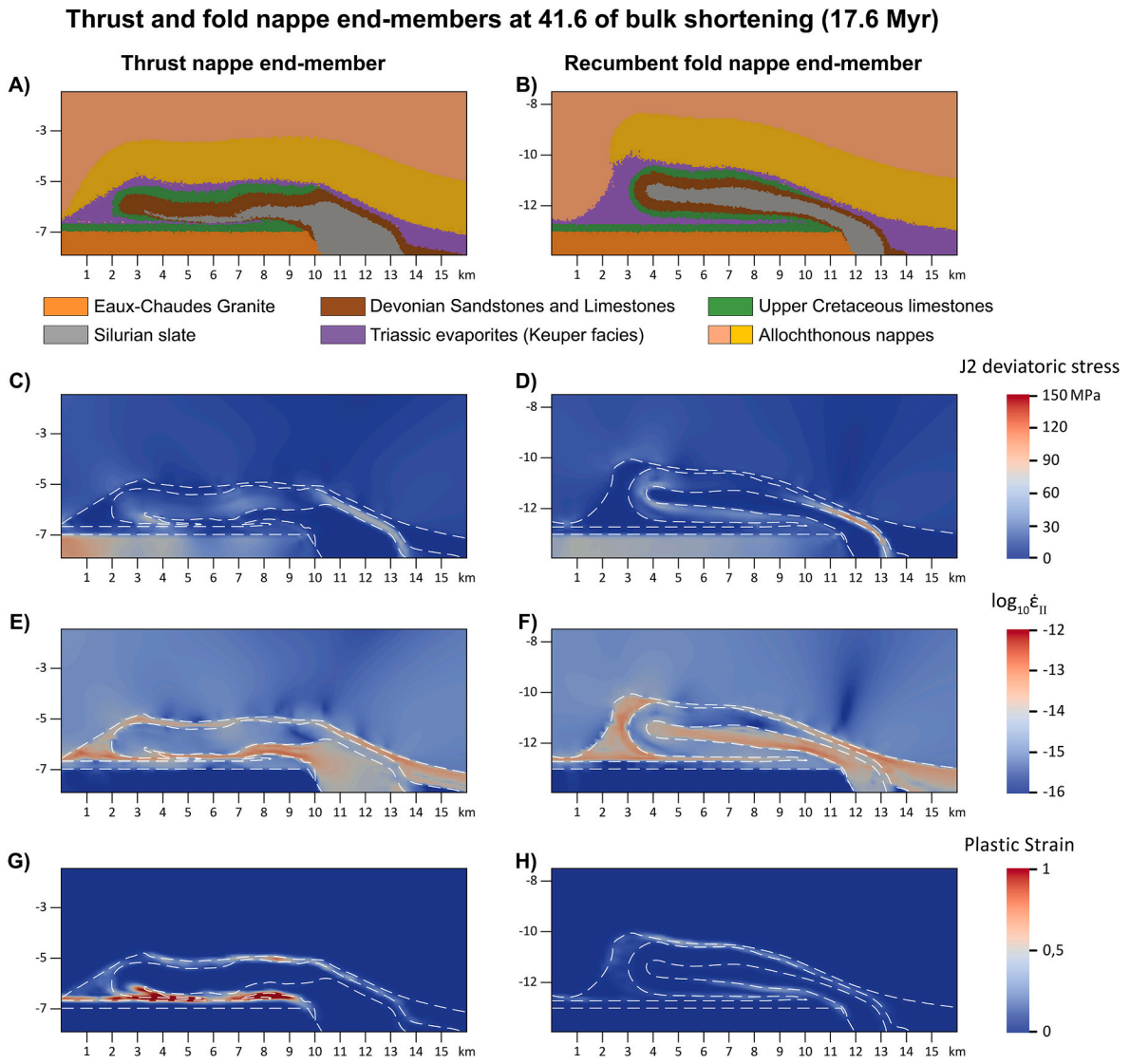

Fig. 14. Final geometry (**A** and **B**), second invariant of the differential stress (**C** and **D**), second invariant of the strain rate tensor (**E** and **F**) and plastic natural strain (**G** and **H**) after 41.6% of shortening for a typical example of a thrust nappe (left; model H_3) and of a recumbent fold nappe (right; model $T_{300}+\beta_{20}$).

similar to the E-C natural example are those formed by a mobile-hinge mechanism (Figs. 8G–I, 11 and 12B, C). However, the scarcity of structural markers confirming mobile hinges challenges a direct comparison of the E-C or other natural examples with the model kinematics, as previously pointed out by Mercier et al. (2007).

Therefore, the interpretation proposed here is that the Eaux-Chaudes fold nappe results from an asymmetric detachment fold developed by limb rotation, with limb overturning during the early deformational steps and later amplified by progressive hinge migration with only moderate stretching of the overturned limb. Epard and Groshong (1995), Homza and Wallace (1997), Poblet and McClay (1996), Perrin et al. (2013) and Poblet (2020) also invoked similar scenarios to describe the migration of fold hinges, with a focus on the migration of the forelimb synclines in thrust tectonics. In the study case, the presence of the strong footwall granitic forestop blocked the migration of syncline hinge and forced the migration of the anticline hinge.

This study is a first approach addressing the influence of the mechanical stratigraphy and the tectonic inheritance. The rheologies considered in our simulations are linear and non-dependent on temperature, which is a simplification. Introducing a non-linear rheology and depth-dependent temperature profile would decrease the effective viscosity and enhance a heterogenous distribution of viscosity during the deformation, and may produce strain localisation at the base of the nappe, as inferred by Bauville et al. (2013). A priori these features could favour the development of the "strain localisation fold nappe" case against the "fold nappe" situation. Complex mechanical coupling with temperature (i.e. thermomechanical), grain size variation (i.e. reduction) or using strain-rate dependent flow laws to simulate rock behaviour may be considered to better understand the processes under which a fold nappe is developed, which will be the object of further studies (e.g. Guardia, 2024).

7. Conclusions

We present mechanical simulations that reproduce the first order features, the structural elements, and the scale of the Eaux-Chaudes case of the Pyrenees and other similar fold nappes. Our modelling also reveals the main mechanical and geometrical factors controlling the formation of thrust nappes vs fold nappes. Modelling results emphasize the need of weak detachment layers above and below the Eaux-Chaudes fold nappe, as well as a stiff footwall forestop to localize deformation, represented by the Eaux-Chaudes granitic pluton.

The E-C recumbent fold nappe was developed between both weak detachments within a low angle shear zone. The thickness of both layers

(Silurian and allochthonous Keuper) is very relevant to allow the detachment of the structure but also to permit the fold growth due to the migration of the hinge and the shear transmission from the Lakora and North Pyrenean overlying nappes. The combination of both decoupling units are essential features favouring viscous behaviour and spatially distributed deformation (low values and stable paths of the localisation index, I_{Loc}), enabling recumbent folding by progressive hinge migration.

Also key was the existence of a forestop, such as the Eaux-Chaudes granite, causing stress concentration in the overlying stiff layers. Model runs without forestop produced detachment buckle folds in the stiff layers, hindering fold nappe development.

The E-C was developed by (1) the plausibility of the migration of the anticline hinge and (2) the rotation of the forelimb followed by the translation of the E-C nappe. The first mechanism is characterized by the continuity of the key layers (Upper Cretaceous and Devonian) and I_{Loc} <0.6, while the second mechanism can be identified by an interrupted key layer (cross-cut by a low angle shear zone) and I_{Loc} >0.6, which is a reflex of an extreme stretching process.

To preserve the overturned limb thickness as observed in the natural case, it is required the migration of the recumbent fold hinge. Otherwise, in scenarios where the migration of hinges is not plausible, the deformation is accommodated by strong stretching and shearing of the reverse limbs.

In the model runs, shallower burial conditions (H), short lengths of the stiff layers (L), lower friction angles of these layers (ϕ), stiffer upper nappes burying the target structure (η_{AN}), and stiffer simulated Upper Cretaceous layer (η_{UC}) hinder hinge migration, enhancing reverse limb stretching and shearing, which eventually results in strain localisation and thrusting (i.e., thrust nappes), well tracked by a rapid increase of the I_{Loc}. It is also evidenced that the intrinsic mechanical properties (ϕ, η_{UC}) of the Upper Cretaceous layer determine whether folding or thrusting dominates. The main features of the initial geometrical configuration and the mechanical properties of the rocks involved in the deformation suggest that both the mechanical and geometrical inheritance are key factors that must not be ignored for an understanding of the alternative development of thrust nappes and fold nappes. The concepts here achieved may apply to other natural examples of recumbent fold nappes (e.g. the Helvetic Alps, with a stiff granite footwall and a weak supra-nappe cover), or to other areas of the Axial Zone of the Pyrenees where recumbent folding could have formed in the upper Paleozoic metasedimentary basement where comparable mechanical and geometrical conditions were attained during the Alpine orogeny.

CRediT authorship contribution statement

Marc Guardia: Writing – original draft, Visualization, Investigation, Conceptualization. **Albert Griera:** Writing – review & editing, Visualization, Investigation, Conceptualization. **Boris J.P. Kaus:** Writing – review & editing, Investigation. **Andrea Piccolo:** Writing – review & editing, Visualization, Investigation, Conceptualization. **Norbert Caldera:** Writing – review & editing, Investigation, Conceptualization. **Antonio Teixell:** Writing – review & editing, Visualization, Investigation, Funding acquisition, Conceptualization.

Declaration of competing interest

The authors declare the following financial interests/personal relationships which may be considered as potential competing interests: Marc Guardia reports financial support was provided by Government of Spain Ministry of Universities. If there are other authors, they declare that they have no known competing financial interests or personal relationships that could have appeared to influence the work reported in this paper.

Acknowledgements

This research was financed by the Spanish MCIU projects PGC2018-093903-B-C21 and PID2021-122467NB-C21. M. Guardia benefitted from an FPU doctoral grant from the Spanish Government. We acknowledge the Johannes-Gutenberg University of Mainz for access to computational infrastructure to run the numerical simulations. We also thank Stefan M. Schmalholz and an anonymous reviewer for comments which helped to improve the manuscript.

Appendix A. Supplementary data

Supplementary data to this article can be found online at https://doi.org/10.1016/j.jsg.2024.105314.

Data availability

Data will be made available on request.

References

Argand, E., 1916. Sur l'arc des Alpes Occidentales. Eclog. Geol. Helvet. 14, 145–191.
Bastida, F., Aller, J., Fernández, F.J., Lisle, R.J., Bobillo-Ares, N.C., Menéndez, O., 2014. Recumbent folds: key structural elements in orogenic belts. Earth Sci. Rev. 135, 162–183. https://doi.org/10.1016/j.earscirev.2014.05.002.
Bauville, A., Epard, J.-L., Schmalholz, S.M., 2013. A simple thermo-mechanical shear model applied to the Morcles fold nappe (Western Alps). Tectonophysics 583, 76–87. https://doi.org/10.1016/j.tecto.2012.10.022.
Bauville, A., Schmalholz, S.M., 2017. Tectonic inheritance and kinematic strain localization as trigger for the formation of the Helvetic nappes, Switzerland. Swiss J. Geosci. 110, 523–534. https://doi.org/10.1007/s00015-017-0260-9.
Bellahsen, N., Jolivet, L., Lacombe, O., Bellanger, M., Boutoux, A., Garcia, S., Mouthereau, F., Le Pourhiet, L., Gumiaux, C., 2012. Mechanisms of margin inversion in the external Western Alps: implications for crustal rheology. Tectonophysics 560–561, 62–83. https://doi.org/10.1016/j.tecto.2012.06.022.
Bucher, W.H., 1956. Role of gravity in orogenesis. Bull. Geol. Soc. Am. 67, 1295–1318. https://doi.org/10.1130/0016-7606(1956)67[1295:ROGIO]2.0.CO;2.
Butler, R., Tavarnelli, E., Grasso, M., 2006. Structural inheritance in mountain belts: an Alpine-Apennine perspective. J. Struct. Geol. 28, 1893–1908. https://doi.org/10.1016/j.jsg.2006.09.006.
Butler, R., Bond, C., Cooper, M.A., Watkins, H., 2018. Interpreting structural geometry in fold-thrust belts: why style matters. J. Struct. Geol. 114, 251–273. https://doi.org/10.1016/j.jsg.2018.06.019.
Caldera, N., Teixell, A., Griera, A., Labaume, P., Lahfid, A., 2021. Recumbent folding in the upper cretaceous Eaux-Chaudes massif: a Helvetic-type nappe in the Pyrenees? Terra. Nova 33, 320–331. https://doi.org/10.1111/ter.12517.
Caldera, N., 2022. Ductile Deformation of the Pyrenean Hinterland during the Alpine Collision: the Case of the Proximal Iberian Margin in the Eaux-Chaudes Massif (West-central Pyrenees), vol. 226. Universitat Autònoma de Barcelona. Doctoral dissertation. http://hdl.handle.net/10803/688310.
Caldera, N., Teixell, A., Griera, A., Labaume, P., Guardia, M., 2023. Alpine ductile deformation of the upper Iberian collided margin (Eaux-Chaudes massif, west-central Pyrenean hinterland, France). Tectonics 42 (11). https://doi.org/10.1029/2023TC007828.
Carreras, J., Druget, E., Griera, A., 2005. Shear zone-related folds. J. Struct. Geol. 27, 1229–1251. https://doi.org/10.1016/j.jsg.2004.08.004.
Choukroune, P., Ecors Team, 1989. The ECORS deep seismic profile reflection data and the overall structure of an orogenic belt. Tectonics 8, 23–29. https://doi.org/10.1029/TC008i001p00023.
Costa, E., Vendeville, B.C., 2002. Experimental insights on the geometry and kinematics of fold-and-thrust belts above weak, viscous evaporitic décollement. J. Struct. Geol. 24 (11), 1729–1739. https://doi.org/10.1016/S0191-8141(01)00169-9.
Dennis, J.G., Price, R.A., Sales, J.K., Hatcher, R., Bally, A.W., Perry, W.J., Laubscher, H. P., Williams, R.E., Elliott, D., Norris, D.K., Hutton, D.W., Emmerr, T., McClay, K.R., 1981. What is a Thrust? What is a Nappe?. In: McClay, K.R., Price, N.J. (Eds.), Thrust and Nappe Tectonics, vol. 9. Geological Society of London Special Publications, pp. 7–9. https://doi.org/10.1144/GSL.SP.1981.009.01.02.
Dietrich, D., Casey, M., 1989. A new tectonic model for the Helvetic nappes. In: Coward, M.P., Park, R.G. (Eds.), Alpine Tectonics, vol. 45. Geological Society London Special Publications, London, pp. 47–63. https://doi.org/10.1144/GSL.SP.1989.045.01.03.
Epard, J.-L., Groshong, R.H., 1995. Kinematic model of detachment folding including limb rotation, fixed hinges and layer-parallel strain. Tectonophysics 247 (1–4), 85–103. https://doi.org/10.1016/0040-1951(94)00266-C.
Epard, J.-L., Escher, A., 1996. Transition from basement to cover: a geometric model. J. Struct. Geol. 5, 533–548. https://doi.org/10.1016/S0191-8141(96)80022-8.
Erickson, S.G., 1996. Influence of mechanical stratigraphy on folding vs. faulting. J. Struct. Geol. 18 (4), 443–450. https://doi.org/10.1016/0191-8141(95)00064-K.
Escher, A., Masson, H., Steck, A., 1993. Nappe geometry in the western Swiss Alps. J. Struct. Geol. 15, 501–509. https://doi.org/10.1016/0191-8141(93)90144-Y.

Ez, V., 2000. When shearing is the cause of folding. Earth Sci. Rev. 51 (1–4), 155–172. https://doi.org/10.1016/S0012-8252(00)00020-9.
Fernández, F.J., Aller, J., Bastida, F., 2007. Kinematics of a kilometric recumbent fold: the Courel syncline (Iberian massif, NW Spain). J. Struct. Geol. 29, 1650–1664. https://doi.org/10.1016/j.jsg.2007.05.009.
Frehner, M., 2011. The neutral lines in buckle folds. J. Struct. Geol. 33 (10). https://doi.org/10.1016/j.jsg.2011.07.005.
Guardia, M., 2024. Time Constraints and Dynamics of the Eaux-Chaudes Nappe (West-Central Pyrenees): A Study Combining New Tectonothermal Data and Thermos-Mechanic Simulations. Universitat Autònoma de Barcelona, p. 371. PhD Thesis. http://hdl.handle.net/10803/691709.
Heim, 1906. Geologische Nachlese Nr. 18. Die vermeintliche «Gewölbeumbiegung des Nordflügels der Glarner Doppelfalte» südlich vom Klausenpass, eine Selbstkorrektur (inkl. Kartenmaterial). Vierteljahrsschrift der Naturforschenden Gesellschaft Zürich 51 (2 und 3), 403–431.
Heim, A., 1919-1922. Geologie der Schweiz. Tauchnitz, Leipzig, 2 Bde.
Homza, T.X., Wallace, W.K., 1995. Geometric and kinematic models for detachment folds with fixed and variable detachment depths. J. Struct. Geol. 17 (4), 575–588. https://doi.org/10.1016/0191-8141(94)00077-D.
Homza, T.X., Wallace, W.K., 1997. Detachment folds with fixed hinges and variable detachment depth, northeastern Brooks Range, Alaska. J. Struct. Geol. 19 (3–4), 337–354. https://doi.org/10.1016/S0191-8141(96)00118-6.
Jammes, S., Manatschal, G., Lavier, L., Masini, E., 2009. Tectonosedimentary evolution related to extreme crustal thinning ahead of a propagating ocean: example of the western Pyrenees. Tectonics 28, 1–24. https://doi.org/10.1029/2008TC002406.
Kaus, B.J.P., Popov, A., Baumann, T., Püsök, A., Bauville, A., Fernandez, N., Collignon, M., 2016. Forward and inverse modelling of Lithospheric deformation on geological timescales. In: NIC Symposium 2016 – Proceedings, Jülich, Germany, NIC Series, vol. 48, pp. 299–307.
Kiss, D., Duretz, T., Schmalholz, S.M., 2020. Tectonic inheritance controls nappe detachment, transport and stacking in the Helvetic nappe system, Switzerland: insights from thermomechanical simulations. Solid Earth 11, 287–305. https://doi.org/10.5194/se-11-287-2020.
Labaume, P., Meresse, F., Jolivet, M., Teixell, A., Lahfid, A., 2016. Tectonothermal history of an exhumed thrust-sheet-top basin: an example from the south Pyrenean thrust belt. Tectonics 35, 1280–1313. https://doi.org/10.1002/2016TC004192.
Labaume, P., Teixell, A., 2020. Evolution of salt structures of the Pyrenean rift (Chaînons Béarnais, France): from hyper-extension to tectonic inversion. Tectonophysics 785, 228451. https://doi.org/10.1016/j.tecto.2020.228451.
Lagabrielle, Y., Labaume, P., S. Blanquat, M., 2010. Mantle exhumation, crustal denudation, and gravity tectonics during Cretaceous rifting in the Pyrenean realm (SW Europe): insights from the geological setting of the lherzolite bodies. Tectonics 29, 1–26. https://doi.org/10.1029/2009TC002588.
Llorens, M.-G., Bons, P.D., Griera, A., Gomez-Rivas, E., Evans, L.A., 2013. Single layer folding in simple shear. J. Struct. Geol. 50, 209–220. https://doi.org/10.1016/j.jsg.2012.04.002.
Lugeon, M., 1902. Les grandes nappes de recouvrement des Alpes du Chablais et de la Suisse. Bull. de la Soc. Geol. Française 4, 723–825.
Manatschal, G., Chenin, P., Lescoutre, R., Miró, J., Cadenas, P., Saspiturry, N., Masini, E., Chevrot, S., Ford, M., Jolivet, L., Mouthereau, F., Thinon, I., Issautier, B., Calassou, S., 2021. The role of inheritance in forming rifts and rifted margins and building collisional orogens: a Biscay-Pyrenean perspective. Bull. Soc. Geol. Fr. 192 (1), 55. https://doi.org/10.1051/bsgf/2021042.
Mancktelow, N.S., 1999. Finite-element modelling of single-layer folding in elasto-viscous materials: the effect of initial perturbation geometry. J. Struct. Geol. 21 (2). https://doi.org/10.1016/S0191-8141(98)00102-3.
Mase, G.E., Mase, G.T., 1970. Continuum Mechanics. McGraw-Hill, New York, p. 398.
Mercier, E., Rafini, S., Ahmadi, R., 2007. Folds kinematics in “fold-and-thrust belts” the “hinge migration” question, a review. In: Lacombe, O., Roure, F., Lavé, J., Vergés, J. (Eds.), Thrust Belts and Foreland Basins. Frontiers in Earth Sciences. Springer, Berlin, Heidelberg. https://doi-org.are.uab.cat/10.1007/978-3-540-69426-7_7.
Muñoz, J.A., 1992. Evolution of a continental collision belt: ECORS-Pyrenees crustal balanced cross-section. In: McClay, K.R. (Ed.), Thrust Tectonics. Springer, Netherlands, pp. 235–246. https://doi.org/10.1007/978-94-011-3066-0_21, 235-246.
Niemeijer, A.R., Spiers, C.J., 2005. Influence of phyllosilicates on fault strength in the brittle-ductile transition: insights from rock analogue experiments. Geol. Soc. London Geol. Soc., London, Spec. Publ. 245 (1), 303–327. https://doi.org/10.1144/GSL.SP.2005.245.01.15.
Perrin, C., Clemenzi, L., Malavieille, J., Molli, G., Taboada, A., Domínguez, S., 2013. Impact of erosion and décollements on large-scale faulting and folding in orogenic wedges: analogue models and case studies. J. Geol. Soc. 170, 893–904. https://doi.org/10.1144/jgs2013-012.
Pfiffner, O.A., 1993. The structure of the Helvetic nappes and its relation to the mechanical stratigraphy. J. Struct. Geol. 15, 511–521. https://doi.org/10.1016/0191-8141(93)90145-Z.
Pfiffner, O.A., 2014. Geology of the Alps. John Wiley and Sons, Chichester, p. 376.
Poblet, J., McClay, K., 1996. Geometry and kinematics of single-layer detachment folds. AAPG (Am. Assoc. Pet. Geol.) Bull. 80 (7), 1085–1109. https://doi.org/10.1306/64ED8CA0-1724-11D7-8645000102C1865D.
Poblet, J., 2020. Cartographic pattern of terminations of simple, parallel fault-bend folds, fault-propagation folds and detachment folds. J. Struct. Geol. 138, 104135. https://doi.org/10.1016/j.jsg.2020.104135.
Ramsay, J.G., 1980. Shear zone geometry: a review. J. Struct. Geol. 2, 83–99. https://doi.org/10.1016/0191-8141(80)90038-3.
Ramsay, J.G., Casey, M., Kligfield, R., 1983. Role shear in the development of the Helvetic fold-and-thrust belt of Switzerland. Geology 11 (8), 439–442. https://doi.org/10.1130/0091-7613(1983)11<439:ROSIDO>2.0.CO;2.
Sornette, A., Davy, P., Sornette, D., 1993. Fault growth in brittle-ductile experiments and the mechanics of continental collisions. J. Geophys. Res. Solid Earth 98, 12111–12139. https://doi.org/10.1029/92JB01740.
Spitz, R., Bauville, A., Epard, J.-L., Kaus, B.J.P., Popov, A., Schmalholz, S.M., 2020. Control of 3D tectonic inheritance on fold-and-thrust belts: insights from 3D numerical models and application to the Helvetic nappe system. Solid Earth 11, 999–1026. https://doi.org/10.5194/se-2019-173.
Teixell, A., 1993. Coupe géologique du massif d’Igountze: implications sur l’évolution structural de la bordure sud de la Zone nord-pyrénéenne occidentale. Comp. Rendus de l’Acad. des Sci., Paris 316, 1789–1796.
Teixell, A., 1998. Crustal structure and orogenic material budget in the west central Pyrenees. Tectonics 17 (3), 395–406. https://doi.org/10.1029/98TC00561.
Teixell, A., Labaume, P., Lagabrielle, Y., 2016. The crustal evolution of the west-central Pyrenees revisited: inferences from a new kinematic scenario. Compt. Rendus Geosci. 348, 257–267. https://doi.org/10.1016/j.crte.2015.10.010.
Termier, P., 1906. La synthèse géologique des Alpes. Imprimerie Moderne 29.
Ternet, 1965. Étude du synclinal complexe des Eaux-Chaudes (Basses-Pyrénées). In: Thèse Doctorat 3° Cycle: Faculté des sciences de l’Université de Toulouse, p. 332.
Turcotte, D., Schubert, J., 2014. Geodynamics. Cambridge University Press, p. 636.
Wallis, D., Lloyd, G.E., Phillips, R.J., Parsons, A.J., Walshaw, R.D., 2015. Low effective fault strength due to frictional viscous flow in phyllonites, Karakoram Fault Zone, NW India. J. Struct. Geol. 77, 45–61. https://doi.org/10.1016/j.jsg.2015.05.010.
Welbon, A., 1988. The influence of intrabasinal faults on the development of a linked thrust system. Geol. Rundschau 77, 11–24. https://doi.org/10.1007/BF01848673.
Wissing, S.B., Pfiffner, O.A., 2003. Numerical models for the control of inherited basin geometries on structures and emplacement of the Klippen nappe (Swiss Prealps). J. Struct. Geol. 25, 1213–1227. https://doi.org/10.1016/S0191-8141(02)00159-1.
Zerlauth, M., Ortner, H., Pomella, H., Pfiffner, O.A., Fügenschuh, B., 2014. Inherited tectonic structures controlling the deformation style: an example from the Helvetic nappes of the Eastern Alps. Swiss J. Geosci. 107, 157–175. https://doi.org/10.1007/s00015-014-0167-7.